Instabilities and Multiscale Interactions Underlying the Loop Current Eddy Shedding in the Gulf of Mexico

YANG YANG

School of Marine Sciences, Nanjing University of Information Science and Technology, Nanjing, China, and College of Marine Science, University of South Florida, St. Petersburg, Florida

ROBERT H. WEISBERG AND YONGGANG LIU

College of Marine Science, University of South Florida, St. Petersburg, Florida

X. SAN LIANG

School of Marine Sciences, School of Atmospheric Sciences, and Center for Ocean–Atmosphere Dynamical Studies, Nanjing University of Information Science and Technology, Nanjing, China

(Manuscript received 19 August 2019, in final form 2 March 2020)

ABSTRACT

A recently developed tool, the multiscale window transform, along with the theory of canonical energy transfer is used to investigate the roles of multiscale interactions and instabilities in the Gulf of Mexico Loop Current (LC) eddy shedding. A three-scale energetics framework is employed, in which the LC system is reconstructed onto a background flow window, a mesoscale eddy window, and a high-frequency eddy window. The canonical energy transfer between the background flow and the mesoscale windows plays an important role in LC eddy shedding. Barotropic instability contributes to the generation/intensification of the mesoscale eddies over the eastern continental slope of the Campeche Bank. Baroclinic instability favors the growth of the mesoscale eddies that propagate downstream to the northeastern portion of the well-extended LC, eventually causing the shedding by cutting through the neck of the LC. These upper-layer mesoscale eddies lose their kinetic energy back to the background LC through inverse cascade processes in the neck region. The deep eddies obtain energy primarily from the upper layer through vertical pressure work and secondarily from baroclinic instability in the deep layer. In contrast, the canonical energy transfer between the mesoscale and the high-frequency frontal eddy windows accounts for only a small fraction in the mesoscale eddy energy balance, and this generally acts as a damping mechanism for the mesoscale eddies. A budget analysis reveals that the mesoscale eddy energy gained through the instabilities is balanced by horizontal advection, pressure work, and dissipation.

1. Introduction

As an integral part of the western boundary current in the North Atlantic Ocean, the Loop Current (LC) enters the Gulf of Mexico (GoM) through the Yucatan Channel, meanders anticyclonically in the eastern basin, and exits through the Straits of Florida (Fig. 1). Large warm anticyclonic rings episodically detach from the LC with diameters of about 300 km and then slowly propagate westward into the western basin. These pinched-off rings are called LC eddies (LCEs). The LC and its associated eddies greatly influence both local hydrology and ecosystem functionality (e.g., Fratantoni et al. 1998; He and Weisberg 2003; Vukovich 2007; Walker et al. 2011; Meza-Padilla et al. 2019), and they leave significant imprints on the overlying atmosphere through air–sea interactions (e.g., Hong et al. 2000; Molina et al. 2016; Jaimes et al. 2016; Shay 2019).

Following the seminal works of Reid (1972) and Hurlburt and Thompson (1980), the accumulation of data from satellite altimeter measurements and in situ observations led to great improvements in describing

---

Supplemental information related to this paper is available at the Journals Online website: https://doi.org/10.1175/JPO-D-19-0202.s1.

Corresponding author: Yang Yang, yangyang2@mail.usf.edu

DOI: 10.1175/JPO-D-19-0202.1

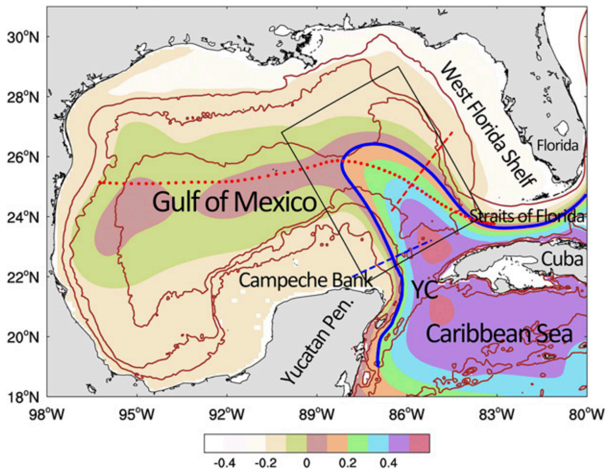

FIG. 1. Mean SSH (color shading; m) in the GoM. The brown contours represent the 100-, 1000-, and 3000-m isobaths. The black-outlined rectangle indicates the LC region in which area-integrated energetics are calculated in Figs. 15–17. The blue solid line and red dotted line indicate the paths used to draw the Hovmöller diagrams in Figs. 4a and 4b, respectively. The blue and red dashed lines indicate the two cross sections examined in Fig. 12.

and understanding the spatiotemporal characteristics of the LC and its detached LCEs during the past few decades (e.g., Molinari et al. 1978; Sturges and Leben 2000; Leben 2005; Vukovich 2007; Hamilton et al. 2016; Liu et al. 2016b; Lugo-Fernández et al. 2016; Weisberg and Liu 2017; Chiri et al. 2019). The LCEs are observed to shed at irregular intervals ranging from 0.5 to 18.5 months (e.g., Vukovich 2007; Sturges and Leben 2000; Leben 2005; Lugo-Fernández and Leben 2010), and they often experience several detachments and reattachments before finally separating from the parent flow. In addition to the LCEs, observations also reveal abundant cyclonic features in the eastern gulf. These cyclonic eddies or meanders are found to make important contributions to the eddy-shedding processes (Cochrane 1972; Vukovich and Maul 1985; Fratantoni et al. 1998; Schmitz 2005; Chérubin et al. 2006; Oey 2008; Walker et al. 2009; Le Hénaff et al. 2012; Huang et al. 2013; Androulidakis et al. 2014; Rudnick et al. 2015; Hamilton et al. 2016).

Different mechanisms have been proposed for the LCE shedding phenomenon. In general, these can be divided into two groups. The first group considers the shedding as deterministic, consistent with the classical Pichevin–Nof theory that interprets eddy shedding as a result of the northward-flowing LC turning eastward to conserve momentum (Pichevin and Nof 1997; Nof 2005). For instance, using a reduced-gravity model, Chang and Oey (2013) argued that the expansion, eddy shedding, and retraction of LC are closely related to the mass and vorticity fluxes at the Yucatan Channel which are largely controlled by wind forcing in the Caribbean Sea. Although several studies emphasize a casual relation between the LCE shedding and upstream perturbations from the Caribbean Sea (e.g., Murphy et al. 1999; Candela et al. 2002; Oey 2004; Athié et al. 2012), such relation does not appear to be statistically robust in long, observation-based time series. Thus, a triggering mechanism remains controversial, even for the sign of a vorticity anomaly that may lead to the expansion and retraction of the LC (Sheinbaum et al. 2016).

The second group suggests that intrinsic ocean processes play an important role in the eddy shedding processes. Because of its high nonlinearity and intermittence, the LC's direct response to external forcing, as identified in idealized models, becomes more ambiguous both in more complete general circulation models and in nature. As a pioneering modeling study, Hurlburt and Thompson (1980) showed that the LC could shed realistic eddies at a quasi-annual period even with steady Yucatan Channel inflow, suggesting that the LC could possibly generate variabilities intrinsically through nonlinear processes such as instabilities and eddy–mean flow interactions. Previous studies based on observations and numerical simulations have provided evidences that baroclinic instability is responsible for the formation of the LCEs (Oey 2008; Xu et al. 2013; Donohue et al. 2016; Hamilton et al. 2019). For example, using observed records from an array of moored current meters and bottom mounted pressure-recording inverted echo sounders, Donohue et al. (2016) and Hamilton et al. (2016) showed that the separations of three observed LCEs were all preceded by the squeezing of a steepening cyclonic meander around the neck of the LC (as pointed out by Schmitz 2005), during which the LC system had strong baroclinic instability that led to a significant increase of mesoscale energy in the local basin, including the lower layer below ~1000 m.

As the dominant circulation feature of the GoM, the LC system has a broad band of spatiotemporal variability. Besides the abovementioned cyclonic eddies which belong to typical variabilities on the mesoscale range in the ocean, recent mooring observations and high-resolution regional models have revealed a rich population of high-frequency frontal eddies along the LC edges (Donohue et al. 2016; Sheinbaum et al. 2016; Jouanno et al. 2016). These high-frequency synoptic (periods <20 days) and small horizontal-scale (<100 km) wavelike motions, which are absent in the current generation of satellite altimetry products, may have important impact on lower-frequency variabilities through inverse cascades of kinetic energy (Sérazin et al. 2018; Yang and Liang 2019a).

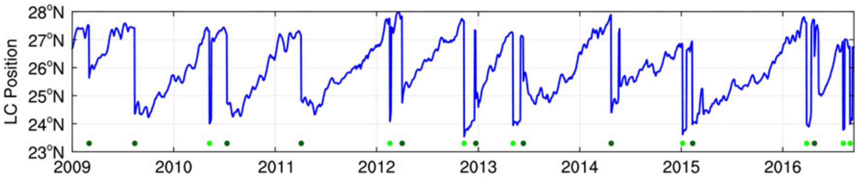

FIG. 2. Time series of the LC position from the GoM forward model. The LC position is defined as the northernmost location of the LC axis (defined as the 17-cm SSH contour) between 94° and 81.5°W. The steric part of the SSH, which is defined as the area mean of the SSH over the GoM, is removed before the calculation. The green dots indicate the time of eddy detachments in the model, with the dark-green ones marking the final detachments.

While several previous studies have examined the two-way interaction between the mean flow and the mesoscale eddies (Oey 2008; Alvera-Azcárate et al. 2009; Donohue et al. 2016), up to now, no work addresses the relative contribution from the mesoscale eddy–mean flow and mesoscale eddy–frontal-scale eddy interactions to the LCE growth and separation in this region. Also unclear are the relative contributions from baroclinic and barotropic instabilities as well as other sources to the eddy energy production during the formation of the LCEs. These issues, among others, motivate us to investigate the dynamics of the LCE shedding from a multiscale energetics point of view. The physical mechanisms responsible for the detachment of the anticyclone from the parent LC will be examined with a high-resolution GoM state estimate developed by the Estimating the Circulation and Climate of the Ocean (ECCO) consortium. The rest of the paper is organized as follows: we first briefly describe the model output in section 2, then introduce the novel three-scale energetics framework (section 3 and 4). The major results are presented in sections 5 and 6, followed by a summary in section 7.

2. The diagnosed simulation

A difficulty in assessing energetics from in situ observations lies in the limitation of spatial and temporal coverage, and, as mentioned in the introduction, the information obtained from satellite altimetry is limited to the sea surface and does not resolve small-scale frontal eddies. Therefore, we use output from an 8-yr-long eddy-resolving ocean model simulation conducted with a regional Massachusetts Institute of Technology general circulation model (MITgcm). The MITgcm is a primitive equation, Boussinesq approximation ocean model formulated with a staggered Arakawa C grid in the horizontal and a z coordinate in the vertical (Marshall et al. 1997). The regional configuration tailored for the GoM domain has been developed over many years to provide a faithful state estimation of the LC and its associated LCE shedding (Gopalakrishnan et al. 2013a,b; Hoteit et al. 2013; Rudnick et al. 2015). Horizontally, the model uses a telescopic grid projection with spacing varying from 5 km in the GoM basin to 10 km near the boundaries, which is sufficient to resolve the small-scale frontal eddies (horizontal size of <100 km). Vertically, the grid consists of 80 levels to attain a high resolution in the upper ocean (37 vertical levels in the upper 1000 m). The initial and lateral boundary conditions are provided by the HYCOM/NCODA global analysis (acronym expansions/definitions can be found at https://www.ametsoc.org/PubsAcronymList), and atmospheric forcing is obtained from the NCEP–NCAR atmospheric reanalysis. A more thorough description of the model configuration can be found online (http://www.ecco.ucsd.edu/gom.html) and in Gopalakrishnan et al. (2013a). The model solution used in the present study is a forward integration from the GoM state estimate project. Since no data are assimilated to interrupt the forward run, the model outputs are kinematically and dynamically consistent, and hence are suitable for energy budget analyses. It should be mentioned that, due to the complexity of the LC system, it is almost impossible for a non-data-assimilative model to capture every observed shedding event in a single multiyear run. However, several key features of the LC are found to be well reproduced in the model. For instance, the spatial patterns of the modeled time-mean surface circulation and the eddy kinetic energy (EKE) are very similar to those from observations (not shown). A total of 10 separation events are identified in the 8-yr model record (Fig. 2). The time period between two consecutive separations ranges from 5.5 to 14.7 months, consistent with satellite observations (e.g., Sturges and Leben 2000; Vukovich 2007). In addition, as will be shown in section 4, there is a good agreement between the dominant sea surface circulation modes of the model and the observation. It is worth noting that the model is found to underestimate the EKE below 1000 m by a factor of approximately 2 (Morey et al. 2020). Such a discrepancy is also found in other regional models such as the (1/25)° data-assimilating GoM Hybrid Coordinate Ocean Model (HYCOM31.0) (Rosburg et al. 2016). It may result from multiple causes related to the model configurations, which is beyond the scope of the present study. In section 5, we will show that the model also exhibits the deep paired anticyclone–cyclone mean circulation underneath the mean LC. Besides, the temporal evolution of the deep EKE is also consistent with observations. These results suggest that the model outputs are suitable for the purpose of this study.

3. The three-scale energetics framework

The Lorenz energy cycle (Lorenz 1955) is an important concept which helps to understand the scale interactions and instabilities in geophysical fluid dynamics (GFD) (e.g., Brooks and Niiler 1977; Weisberg and Weingartner 1988; Liang and Robinson 2005, 2007; von Storch et al. 2012; Liang 2016; Yang and Liang 2019b). The traditional energetics framework as formulated by Lorenz is based on a Reynolds' mean–eddy decomposition, and hence only describes the steady-state budget of mechanical energy in a two-scale sense. It is difficult to distinguish among the relative contributions to motions with nonstationary background by those with multiple time scales. As mentioned in the introduction, the LC system involves processes on a range of scales, or scale windows, a term introduced by Liang and Anderson (2007). At least three scale windows may be defined for the flow system in the eastern GoM, that is, nonstationary background flow window, mesoscale eddy window, and high-frequency frontal eddy window.

We use the multiscale window transform (MWT), developed by Liang and Anderson (2007), to fulfill the scale decomposition. MWT is a functional analysis apparatus that decomposes a function space into a direct sum of orthogonal scale windows while retaining information regarding its locality (in this study, temporal locality); it is developed for a faithful representation of localized multiscale energies on the resulting scale windows (Liang and Anderson 2007; Liang 2016). As an example, consider a field $u = u(t)$ (spatial dependence suppressed for simplicity) which is a square integrable function defined on [0, 1] (if not, the domain can always be rescaled to [0, 1]). Now suppose that $\{\phi_n^j(t)\}_n$ is an orthonormal translational invariant scaling sequence [built from cubic splines; see Liang and Anderson (2007) for details], with j being some wavelet time scale level and n being the discrete time step in the sampling space. Using $\{\phi_n^j(t)\}_n$ as a basis, there is a scaling transform

$$\hat{u}_n^j = \int_0^1 u(t)\phi_n^j(t)\,dt \tag{1}$$

for any scale level j (corresponding to frequency 2^j). Given window bounds $j_0 < j_1 < j_2$ for a three-scale-window decomposition, u then can be reconstructed by the three windows:

$$u^{\sim 0}(t) = \sum_{n=0}^{2^{j_0}-1} \hat{u}_n^{j_0}\phi_n^{j_0}(t), \tag{2}$$

$$u^{\sim 1}(t) = \sum_{n=0}^{2^{j_1}-1} \hat{u}_n^{j_1}\phi_n^{j_1}(t) - u^{\sim 0}(t), \quad \text{and} \tag{3}$$

$$u^{\sim 2}(t) = u(t) - u^{\sim 0}(t) - u^{\sim 1}(t), \tag{4}$$

with the notations ~ 0, ~ 1, and ~ 2 respectively signifying the nonstationary background flow window, mesoscale eddy window, and high-frequency frontal eddy window. These scale-window reconstructions correspond to the well-known low-pass-, bandpass-, and high-pass-filtered fields in the traditional sense. With these reconstructions, the MWT of u is defined as

$$\hat{u}_n^{\sim\varpi} = \int_0^1 u^{\sim\varpi}(t)\phi_n^{j_2}(t)\,dt \tag{5}$$

for windows $\varpi = 0, 1, 2$, and $n = 0, 1, \ldots, 2^{j_2} - 1$. Hence, Eqs. (2)–(4) can be written in a unified way:

$$u^{\sim}(t) = \sum_{n=0}^{2^{j_2}-1} \hat{u}_n^{\sim\varpi}\phi_n^{j_2}(t), \quad \varpi = 0, 1, 2. \tag{6}$$

A natural question to ask is, What is the energy of a multiscale reconstructed field (filtered field) $u^{\sim\varpi}(t)$? During the past decades, a common practice is simply taking the square of $u^{\sim\varpi}(t)$, that is, $[u^{\sim\varpi}(t)]^2$ (up to some constant factor). This is, however, conceptually wrong. Multiscale energy is a concept in phase space (think about the Fourier power spectrum), while $[u^{\sim\varpi}(t)]^2$ is a quantity in physical space! In fact, this is a very fundamental and difficult problem in functional analysis; it is by no means as trivial as it has been treated in atmosphere–ocean science. Liang and Anderson (2007) found that, for certain type of orthogonal filters, there exists a transform–reconstruction pair, just as the transfer-inverse transform in Fourier analysis. That is to say, corresponding to each reconstruction $u^{\sim\varpi}(t)$, there exists a transform coefficient $\hat{u}_n^{\sim\varpi}$. In the MWT framework, the energy on scale window $\varpi = (0, 1, 2)$ proves to be $(\hat{u}_n^{\sim\varpi})^2$ (up to some factor). The reader is referred to Liang and Anderson (2007) for technical details about MWT and to Liang (2016) for more details on the time-dependent energy representation problem.

Previous studies have shown that mesoscale variabilities within 100–40 day band play an important role in the LCE detachments (e.g., Donohue et al. 2016; Hamilton et al. 2016). In this study, the mesoscale eddy window is chosen to be bounded by cutoff periods of 180 and 20 days. Processes with periods longer than 180 days (including the time mean) are defined as the nonstationary background flow. The residual high-frequency signals are treated as LC frontal eddies, in accordance with Jouanno et al. (2016). Caution should be taken when selecting the lower-frequency bound for the mesoscale window (i.e., 180 days in this study). It should not be longer than 200 days since the leading mode of the upper-layer circulation, which represents the growth and wane of the LC, has a dominant period around 200–350 days (see section 4 for details). Inclusion of those low-frequency dominant signals into the mesoscale eddy window will lead to an unfaithful representation of the eddy energetics in this particular region. In Fig. 3, we plot the MWT-reconstructed sea surface height (SSH) snapshots from December 2011 to April 2012 during which a typical shedding event occurred. The background flow in our framework shows the northward extension and ‘‘necking-down’’ of the LC during the considered period (color shading in Fig. 3b). After subtracting the time-mean over the entire simulation period, the anomaly field on this window depicts a wavelike pattern propagating northwestward (see the black contours in Fig. 3b and the Hovmöller diagram in Fig. 4a). Note that these westward propagating anomalies are not equivalent to physical eddies; they reflect the low-frequency modulation (growth and wane) of the LC controlled by Rossby wave dynamics as shown in several previous studies (e.g., Hurlburt and Thompson 1982; Chang and Oey 2013; Xu et al. 2013).

In the mesoscale window (Fig. 3c), an elongated cyclonic lobe first appears to the north of the Campeche Bank in early December and moves northward along the LC. From 22 January to 18 February, the cyclonic eddy intensifies while propagating along the east side of the LC and cuts through the neck of LC, leading to the first detachment. Once the LCE reattaches shortly after the first detachment, another cyclonic eddy begins to propagate downstream and intensify. Similar to the previous shedding process, the cyclone propagates southwestward and causes the final separation of the LCE on 8 April 2012. Figure 4 further shows the Hovmöller diagrams of the SSH anomaly on the background and mesoscale window along the blue and red paths shown in Fig. 1. Variabilities on these two scale windows exhibit distinct propagating features; that is, the background anomaly propagates westward (Fig. 4a), consistent with Rossby wave dynamics while the mesoscale anomalies generally propagate along the axis of the LC with a much faster speed (Fig. 4b).

Note that the propagating features in the deep basin (i.e., around 700–1100 km in Fig. 4b) are not as clearly captured by the Hovmöller diagram with a fixed path due to the highly variable path state of the LC in this region. These are clearer when looking at daily snapshots of the mesoscale window (Fig. 3; also see the movie in the online supplemental material).

From Fig. 4b, Fig. 3, and the online supplemental material, we can see that prior to the eddy shedding, the mesoscale features on the west side of the LC (many propagate from the Caribbean Sea) tend to intensify near 22°N (i.e., around 300 km in Fig. 4b) and propagate along the LC axis. Once they approach the eastern side of the LC, they experience another major growth (much more intense than that occurs along the western branch) and they eventually lead to the necking-down of the LC once they migrate southwestward. In section 5, we will identify the key mechanisms responsible for the eddy development in these two particular (western and eastern) regions.

To see the behavior of deep flow during the eddy shedding, we plot the MWT-reconstructed velocity vector snapshots in Fig. 5. The deep flow is dominated by variabilities in the mesoscale band in the eastern basin. Perturbations in the deep layer tend to intensify along with their upper-layer counterparts prior to the eddy shedding. For instance, on 8 February 2012, 10 days before the first detachment, a north-to-south anticyclonic–cyclonic eddy pair is well established underneath the eastern LC periphery. These deep eddies lead the surface-layer eddy pair by about 90° in phase, indicating that the system is baroclinically unstable (Pedlosky 1987). This is a typical scenario from the mesoscale perspective during the course of the LCE shedding, consistent with previous studies using observations or numerical simulations (Schmitz 2005; Rudnick et al. 2015; Donohue et al. 2016; Hamilton et al. 2016). In contrast, the background flow in the deep layer is dominated by a pair of anticyclonic and cyclonic eddies propagating northwestward in the deep basin (Fig. 4b), in phase with the surface SSH anomaly in the background flow window (Fig. 3), indicating a barotropic vertical mode.

Here we remark that the mesoscale cyclonic/anticyclonic features may not be easily observed in the original field due to their relatively smaller amplitude when

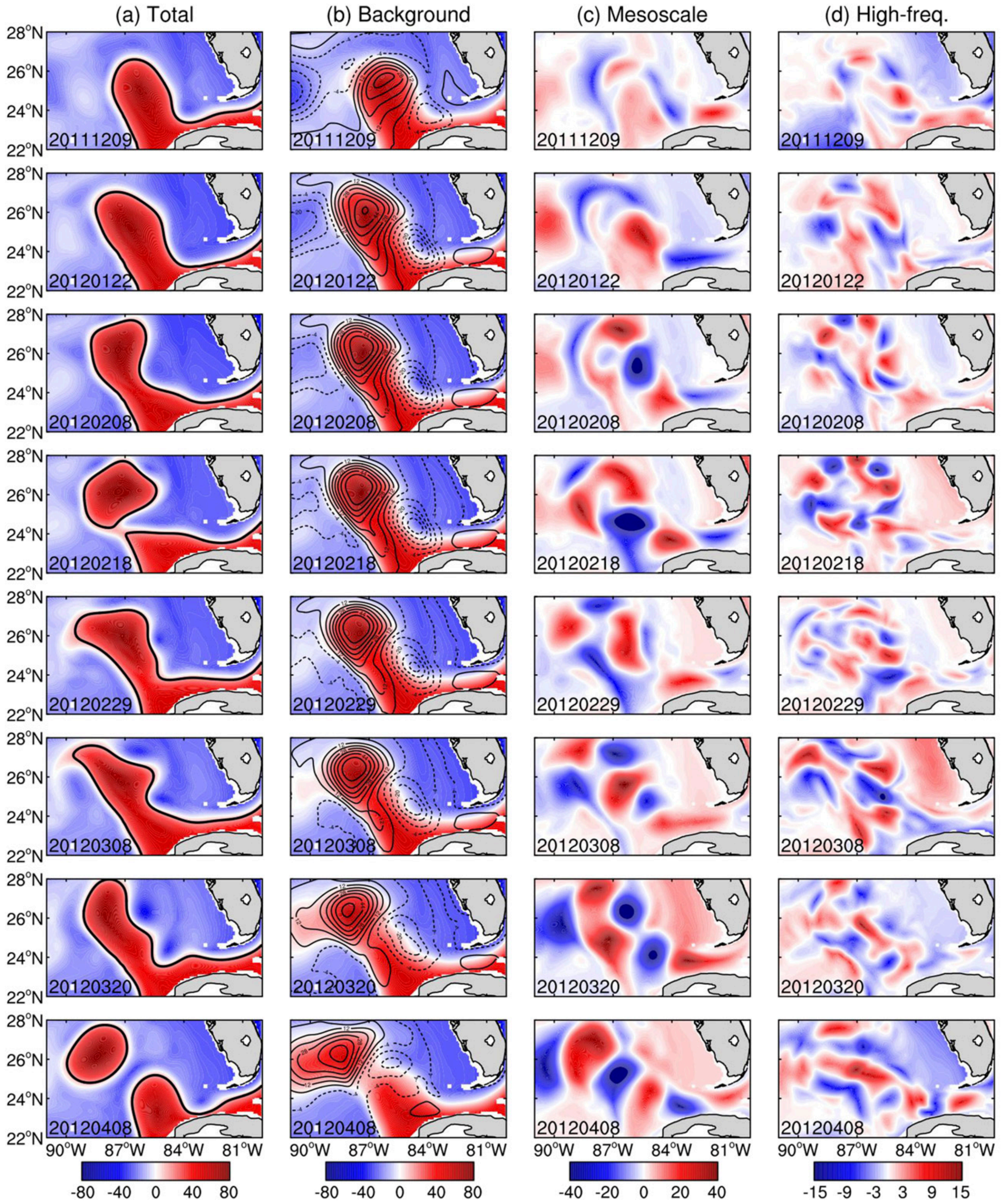

FIG. 3. SSH snapshots (cm) from 9 Dec 2011 to 8 Apr 2012: (a) the original field, (b) the MWT low-pass-filtered field (defined as processes with periods longer than 180 days; referred to as the background flow window in the text), (c) the MWT bandpass-filtered field (defined as processes with periods within 20–180-day bands; referred to as mesoscale window in the text), and (d) the MWT high-pass-filtered field (defined as processes with periods shorter than 20 days; referred to as high-frequency eddy window). The thick black contour in (a) denotes the 17-cm SSH locations, which indicate the LC axis. The black solid or dashed contours superposed in (b) denote the positive or negative SSH anomalies, respectively, on the background flow window (i.e., the time mean over the entire length of simulation is subtracted; see Fig. 1).

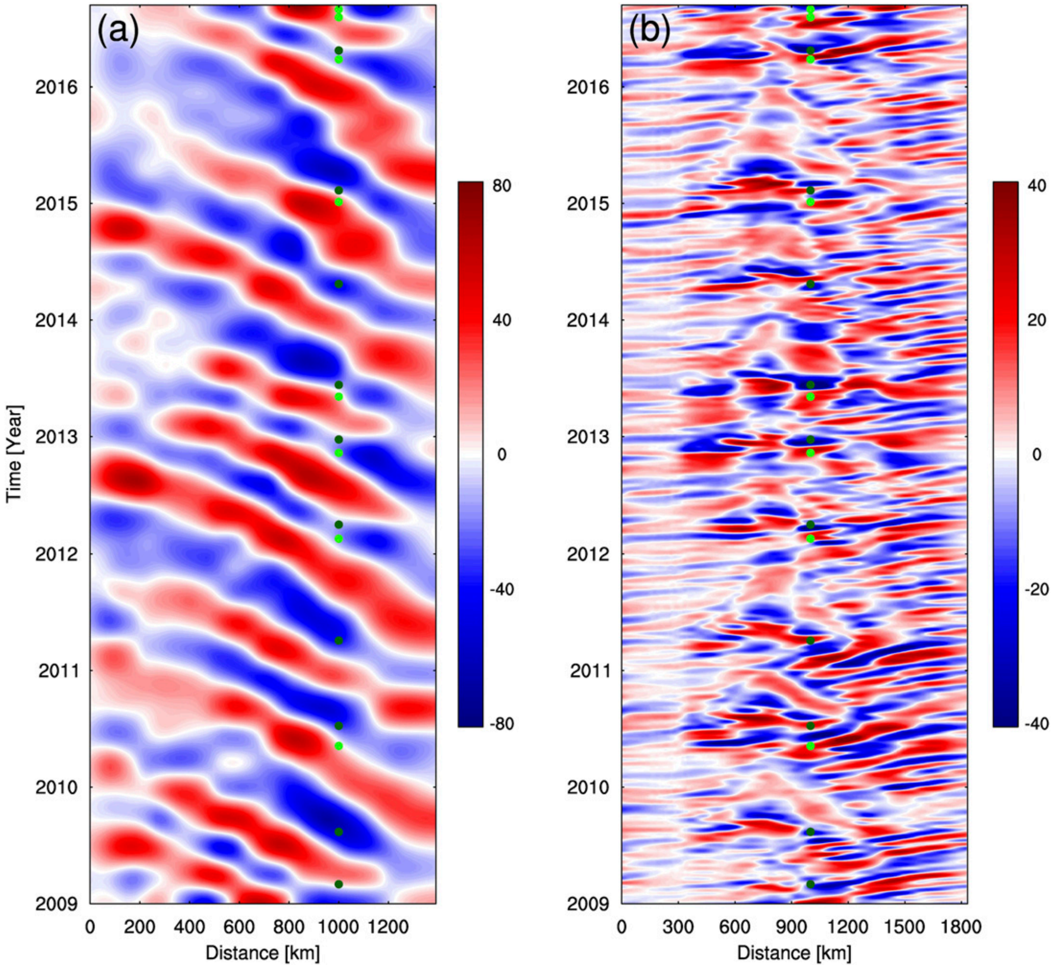

FIG. 4. (a) Hovmöller diagram of the SSH anomaly on the background window along the red dotted line shown in Fig. 1. (b) As in (a), but for the SSH anomaly on the mesoscale flow along the blue line shown in Fig. 1. The green dots are the same as those in Fig. 2. Note that the location of these dots does not reflect the actual position of the shedding.

compared to the dominant LC and LCEs (Fig. 3a), but they are clearly seen in the mesoscale reconstructed maps (Fig. 3c). An interesting observation from these snapshots is that the mesoscale activities tend to grow in phase with the arrival of the anomaly pair of the background flow coming from southeast (associated with the extension of the LC). Also, the upper eddies tend to migrate along the strong anomalous flow between the positive and negative anomalies of the background flow, eventually leading to the eddy detachment. These results indicate a strong coupling of the background flow and the mesoscale motions that affects the eddy shedding.

The small-scale, high-frequency SSH features propagate anticyclonically along the edge of the LC (or along the LCE edge after the detachment; Fig. 3d). Note that these higher-frequency eddies are also indiscernible in the original fields (Fig. 3a). The dynamical coupling between these small eddies and the mesoscale eddies is yet to be determined.

4. Energetics analyses formulation

For a hydrostatic and Boussinesq flow, the primitive equations are

$$\frac{\partial \mathbf{v}_h}{\partial t} + \mathbf{v}\cdot\nabla\mathbf{v}_h + f\mathbf{k}\times\mathbf{v}_h = -\frac{1}{\rho_0}\nabla_h P + F_m, \tag{7}$$

$$\frac{\partial P}{\partial z} = -\rho g, \tag{8}$$

$$\nabla\cdot\mathbf{v} = 0, \quad \text{and} \tag{9}$$

$$\frac{\partial \rho}{\partial t} + \mathbf{v}\cdot\nabla\rho = \frac{\rho_0 N^2}{g} w + F_\rho, \tag{10}$$

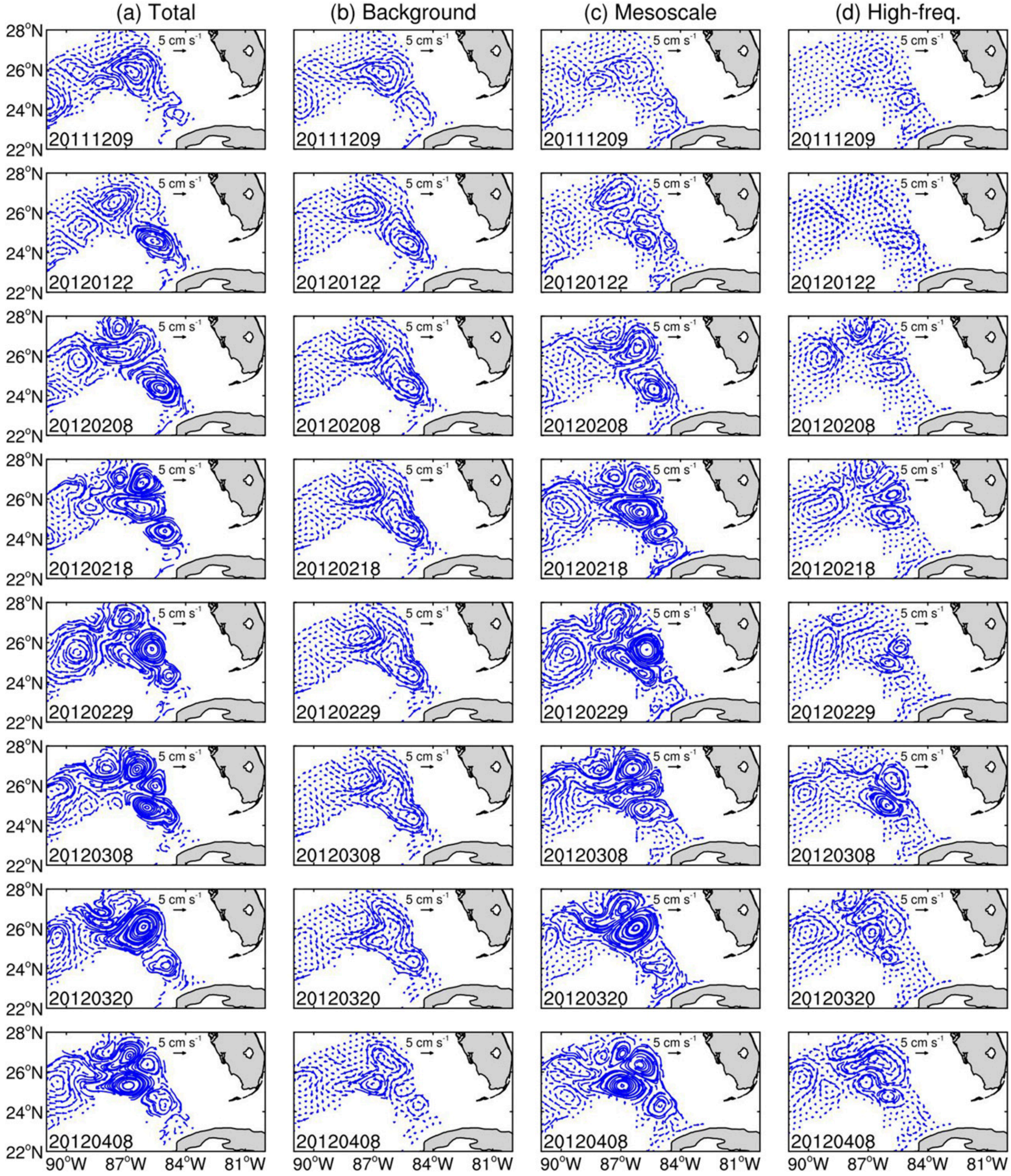

FIG. 5. As in Fig. 3, but for the velocity vectors at 2000-m depth.

where **v** is the three-dimensional velocity vector, ∇ is the three-dimensional gradient operator, and the subscript h denotes their horizontal components. The effects of forcing and dissipation are included in the F terms. Note that ρ is the density anomaly from a reference state $\rho_r(z)$ (chosen to be the time- and area-mean density), and P is the dynamic pressure field related to ρ. The buoyancy frequency N is given by $N^2 = -(g/\rho_0)d\rho_r/dz$. The other notations are conventional.

Based on the MWT, the kinetic energy (KE) and the available potential energy (APE) on scale window ϖ, in units of joules per kilogram, are

$$K^{\varpi} = \frac{1}{2}\hat{\mathbf{v}}_h^{\sim\varpi} \cdot \hat{\mathbf{v}}_h^{\sim\varpi} \quad \text{and} \tag{11}$$

$$A^{\varpi} = \frac{1}{2}c(\hat{\rho}^{\sim\varpi})^2, \tag{12}$$

where the operator $\widehat{(\,)}^{\sim\varpi}$ denotes MWT on window ϖ, and the z-dependent coefficient $c = g^2/\rho_0^2N^2$ is introduced for convenience. Note that these multiscale energies are all functions of n; that is, they are time-dependent variables. For notational brevity, hereinafter, the dependence on n will be suppressed in the MWT terms, unless otherwise indicated. By taking MWT on both sides of Eq. (7), multiplying by $\hat{\mathbf{v}}^{\sim\varpi}$, and separating the nonlinear advection term into a transport and a canonical transfer in a rigorous way (for a detailed derivation, refer to Liang 2016), the time evolution equation for the multiscale KE (K^{ϖ}) can be obtained:

$$\frac{\partial K^{\varpi}}{\partial t} = \underbrace{-\nabla \cdot \left[\frac{1}{2}\widehat{(\mathbf{v}\mathbf{v}_h)}^{\sim\varpi} \cdot \hat{\mathbf{v}}_h^{\sim\varpi}\right]}_{-\nabla\cdot\mathbf{Q}_K^{\varpi}} + \underbrace{\frac{1}{2}\left[\widehat{(\mathbf{v}\mathbf{v}_h)}^{\sim\varpi} : \nabla\hat{\mathbf{v}}_h^{\sim\varpi} - \nabla \cdot \widehat{(\mathbf{v}\mathbf{v}_h)}^{\sim\varpi} \cdot \hat{\mathbf{v}}_h^{\sim\varpi}\right]}_{\Gamma_K^{\varpi}} \underbrace{-\nabla \cdot \left(\frac{1}{\rho_0}\hat{\mathbf{v}}^{\sim\varpi}\hat{P}^{\sim\varpi}\right)}_{-\nabla\cdot\mathbf{Q}_P^{\varpi}} + \underbrace{\left(-\frac{g}{\rho_0}\hat{\rho}^{\sim\varpi}\hat{w}^{\sim\varpi}\right)}_{b^{\varpi}} + F_K^{\varpi}, \tag{13}$$

where the colon represents the colon (or double dot) product of two dyads (cf. Liang 2016). Similarly, the multiscale APE (A^{ϖ}) budget equation can be obtained by taking MWT on both sides of the density equation, multiplying by $c\hat{\rho}^{\sim\varpi}$, and implementing a separation of transport–transfer:

$$\frac{\partial A^{\varpi}}{\partial t} = \underbrace{-\nabla \cdot \left[\frac{1}{2}c\hat{\rho}^{\sim\varpi}\widehat{(\mathbf{v}\rho)}^{\sim\varpi}\right]}_{-\nabla\cdot\mathbf{Q}_A^{\varpi}} + \underbrace{\frac{c}{2}\left[\widehat{(\mathbf{v}\rho)}^{\sim\varpi} \cdot \nabla\hat{\rho}^{\sim\varpi} - \hat{\rho}^{\sim\varpi}\nabla \cdot \widehat{(\mathbf{v}\rho)}^{\sim\varpi}\right]}_{\Gamma_A^{\varpi}} + \underbrace{\left(\frac{g}{\rho_0}\hat{\rho}^{\sim\varpi}\hat{w}^{\sim\varpi}\right)}_{-b^{\varpi}} + \underbrace{\frac{1}{2}\hat{\rho}^{\sim\varpi}\widehat{(w\rho)}^{\sim\varpi}\frac{\partial c}{\partial z}}_{S_A^{\varpi}} + F_A^{\varpi}. \tag{14}$$

In Eqs. (13) and (14), the left-hand-side terms are the local tendency of KE and APE on window ϖ, respectively; they are controlled by the multiple processes on the right-hand side of the two equations. These processes are summarized as follows:

- The $-\nabla \cdot \mathbf{Q}_K^{\varpi}$ and $-\nabla \cdot \mathbf{Q}_A^{\varpi}$ are the convergence (note the minus sign) of the K^{ϖ} and A^{ϖ} flux respectively. These two processes represent the spatial advections of energy on window ϖ and hence are called transports.
- The Γ_K^{ϖ} and Γ_A^{ϖ} are the transfer of KE and APE, respectively, to window ϖ from the other windows. These two processes represent the redistributions of energy across the scale windows. Note that these two terms need to be further decomposed to obtain the window-to-window interactions embedded in the three-scale window framework (see below).
- The b^{ϖ} is the buoyancy conversion on window ϖ, which represents conversion of different types of mechanical energy from one form to another (e.g., K^{ϖ} or A^{ϖ}).
- The $-\nabla \cdot \mathbf{Q}_P^{\varpi}$ is the pressure flux convergence or pressure work.
- The S_A^{ϖ} is the apparent source/sink of A^{ϖ} that is due to the nonlinearity of the reference stratification (usually negligible).
- The residual terms F_K^{ϖ} and F_A^{ϖ} include all of the external forcings (such as the work done by wind stress), friction, and other unresolved subgrid processes.

For convenience, the divergence terms $-\nabla \cdot \mathbf{Q}_K^{\varpi}$, $-\nabla \cdot \mathbf{Q}_A^{\varpi}$, and $-\nabla \cdot \mathbf{Q}_P^{\varpi}$ will be hereinafter written as ΔQ_K^{ϖ}, ΔQ_A^{ϖ}, and ΔQ_P^{ϖ}, respectively. As will be shown later, the vertical component of ΔQ_P^{ϖ} (denoted as $\Delta_z Q_P^{\varpi}$) is essential to couple the eddy energetics in the upper and deep layers and therefore will be diagnosed separately from its horizontal counterpart (denoted as $\Delta_h Q_P^{\varpi}$). In contrast, the vertical components of ΔQ_K^{ϖ} and ΔQ_A^{ϖ} are negligible relative to their horizontal counterparts. Therefore, we treat ΔQ_K^{ϖ} and ΔQ_A^{ϖ} as a whole in this study. It is worth mentioning that all of the terms in Eqs. (13) and (14) are four-dimensional because of the localized nature of MWT, distinctly different from the classical Lorenz-type formalisms (e.g., Lorenz 1955; von Storch et al. 2012) in which localization is lost in at least one dimension of space–time to achieve the scale decomposition. This advantage allows us to investigate the time-varying diagram of the scale interactions and instabilities underlying the eddy shedding processes.

The cross-scale transfers (i.e., Γ_K^{ϖ} and Γ_A^{ϖ}) satisfy the following property:

$$\sum_{\varpi}\sum_{n}\Gamma_n^{\varpi} = 0, \qquad (15)$$

where $\sum_{\varpi}$and $\sum_{n}$sum over all of the sampling time steps n and scale windows ϖ, respectively. This is achieved by a unique separation of energy transfer from the spatial transport with the aid of MWT. Equation (15) states that a transfer process adds up to zero when summing over all windows and time steps, and therefore is merely a redistribution of energy among scale windows, without generating or losing energy as a whole. This property, although simple to state, is not met in classical energetics formalisms. To distinguish, Γ is termed "canonical transfer" (Liang 2016).

Instability, a fundamental GFD concept, is described as the energy transfer from the background flow to the perturbation (Pedlosky 1987). As we mentioned earlier, the energy transfers that appear in traditional energetics formalisms do not conserve energy in the space of scale; they still contain processes which do not cascade across scales, and hence cannot faithfully represent instabilities. As proved by Liang and Robinson (2007), canonical transfer corresponds precisely to GFD instability in the classical sense; it has been validated with a benchmark instability model whose instability structure is analytically known. Note that the canonical transfers (i.e., Γ_K^{ϖ} and Γ_A^{ϖ}) in Eqs. (13) and (14) are still in a cumulated form; they need to be further decomposed to get the window-to-window interactions embedded in the three-scale window framework. This is achieved by a technique called "interaction analysis" (Liang and Robinson 2005). In the following, these window-to-window interactions (and hence instabilities) are signified by superscripts like $0\rightarrow1$, $2\rightarrow1$. For instance, the canonical transfer of KE or APE from the background flow window ($\varpi = 0$) to the mesoscale eddy window ($\varpi = 1$) is denoted as $\Gamma_K^{0\rightarrow1}$ or $\Gamma_A^{0\rightarrow1}$, respectively. A positive $\Gamma_K^{0\rightarrow1}$ or $\Gamma_A^{0\rightarrow1}$ respectively means a release of background flow KE or APE for the growth of mesoscale eddies, which is indicative of the occurrence of barotropic or baroclinic instability, respectively. Thus, these two transfers are also referred to as barotropic and baroclinic canonical transfer, respectively. Similarly, the scale interaction between the high-frequency eddy and the mesoscale eddy is quantified by $\Gamma_K^{2\rightarrow1}$ and $\Gamma_A^{2\rightarrow1}$. A positive $\Gamma_K^{2\rightarrow1}$ or $\Gamma_A^{2\rightarrow1}$ means an inverse cascade of KE or APE, respectively, from the high-frequency eddies to the lower-frequency mesoscale eddies. The above four diagnostics provide the criteria for the two instabilities and scale–scale interactions, allowing us to evaluate the relative importance of barotropic and baroclinic instabilities, and the impact of frontal eddies to the mesoscale eddies associated with the eddy-shedding processes, which otherwise would be difficult, if not impossible, to investigate.

Eddy shedding is essentially about a simultaneous EKE growth on the mesoscale window, associated with joint development of mesoscale anticyclonic–cyclonic eddies in both the upper and deep layers (Sheinbaum et al. 2016; Donohue et al. 2016; Hamilton et al. 2019); we hence focus specifically on the mesoscale eddy window ($\varpi = 1$) energetics, which are written as

$$\frac{\partial K^1}{\partial t} = \Gamma_K^{0\rightarrow1} + \Gamma_K^{2\rightarrow1} + b^1 + \Delta Q_K^1 + \Delta_h Q_P^1 + \Delta_z Q_P^1 + F_K^1 \quad \text{and} \qquad (16)$$

$$\frac{\partial A^1}{\partial t} = \Gamma_A^{0\rightarrow1} + \Gamma_A^{2\rightarrow1} - b^1 + \Delta Q_A^1 + S_A^1 + F_A^1 . \qquad (17)$$

Figure 6 shows a schematic of the energy cycle in the three-scale framework. Summing the above two equations, we can obtain the mechanical energy budget for the mesoscale eddy window:

$$\frac{\partial E^1}{\partial t} = \Gamma_K^{0\rightarrow1} + \Gamma_A^{0\rightarrow1} + \Gamma_E^{2\rightarrow1} + \Delta Q_E^1 + \Delta_h Q_P^1 + \Delta_z Q_P^1 + S_A^1 + F_E^1, \qquad (18)$$

where $E^1 = K^1 + A^1$ is the mechanical energy. These equations will be used in section 5 to investigate the dynamics responsible for the development of the mesoscale eddies and separation of the LCE.

5. Dominant evolution patterns of the mesoscale EKE and circulation in the eastern GoM

To examine how the mesoscale eddy activity and circulation are related in the eastern Gulf, we perform a singular value decomposition (SVD) analysis by analyzing the covariance matrices of the surface total relative vorticity $\zeta = v_x - u_y$ and $K^1 = (1/2)(\hat{\mathbf{v}}_h^1 \cdot \hat{\mathbf{v}}_h^1)$ fields over the eastern basin (21°–29°N, 90°–80°W). SVD analysis is widely used to identify a pair of coupled patterns which explain as much as possible the covariance between two fields (e.g., Bretherton et al. 1992). The two leading modes contain 77.2% of the total square covariance between the two fields (46.5% and 30.7% for the first and second mode, respectively), and

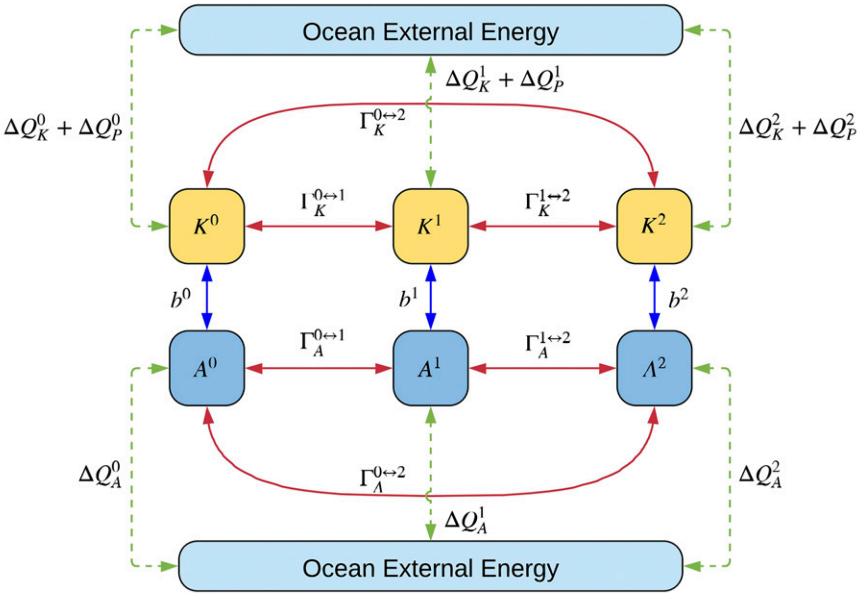

FIG. 6. The energy cycle diagram for a three-window decomposition. Red arrows stand for the canonical transfers, and blue arrows indicate the buoyancy conversions. Green dashed arrows indicate the spatial transport processes (in divergence forms). For clarity, the forcing/dissipation processes in each window are not shown.

these are well separated from the higher modes (the third mode contains only 4.4% of the total covariance). Figure 7 displays the spatial patterns as well as the associated temporal expansion coefficients for the first SVD mode. The vorticity pattern is characterized by a positive anomaly centered at 24.5°N, 86°W, sandwiched by a loop shaped negative vorticity anomaly (color shading in Fig. 7a). The regression pattern of the SSH anomaly (black contours in Fig. 7a) with respect to the vorticity expansion coefficient manifests a train of positive and negative centers between the Straits of Florida and the Mississippi Fan, with the negative or positive SSH anomaly coinciding with positive or negative relative vorticity, respectively. This spatial pattern is similar to the leading empirical orthogonal function eigenvector of SSH as revealed in previous studies (e.g., Chang and Oey 2013; Lin et al. 2010). A wavelet analysis (Liu et al. 2007) shows that the first mode has a main peak of energy at periods around 200–350 days (Fig. 7d), in agreement with previous work (Chang and Oey 2013; Liu et al. 2016b). The first SVD mode of K^1 displays a spatially coherent pattern with positive anomaly over the eastern basin (Fig. 7b). It is found that the mode 1 K^1 expansion coefficient almost coincides with the area-mean K^1 time series (green line in Fig. 7e) averaged over the LC region (see the black-outlined box in Fig. 1), with the correlation coefficient as high as 0.94. This suggests that the first mode of K^1 captures the regional mesoscale EKE variability, which is closely related with the eddy-shedding processes. As can be seen in Fig. 7e (blue line), the simultaneous correlation coefficient between the pair of the two expansion coefficients is 0.7 (significant at 95% level), indicating that the two fields are strongly coupled in this region.

To further reveal the temporal and spatial phase relationships between the mesoscale EKE and the background circulation in this region, we construct lagged regression maps of the SSH anomaly and K^1 fields onto the SVD-1 temporal coefficient of K^1 (Fig. 8). A positive lag means that the SVD-1 K^1 coefficient time series takes the lead. The lagged-regression maps depict the mesoscale EKE evolution associated with the northwestward propagation of the SSH anomaly in the eastern basin. The spatial size of these anomalies is around 300 km, much larger than the mesoscale eddies moving along the LC front as shown in the daily snapshots (Fig. 3c). To see how the migration of these large-scale anomalies is related with the wax and wane of the LC, we add the time mean component to the anomaly patterns to get the total SSH. As shown with the 17-cm SSH contour (green contour in Fig. 8), the LC indeed extends northwestward at lags from −90 to 0 day. An anticyclone is eventually pinched off from the LC at a lag of +50 day, and then the LC slowly retracts to the south. The detachment revealed in the first mode lags the EKE maximum by about 50 days (Fig. 8d), while the burst of mesoscale EKE usually occurs in phase with the eddy shedding processes (see Fig. 7c). This is because the first

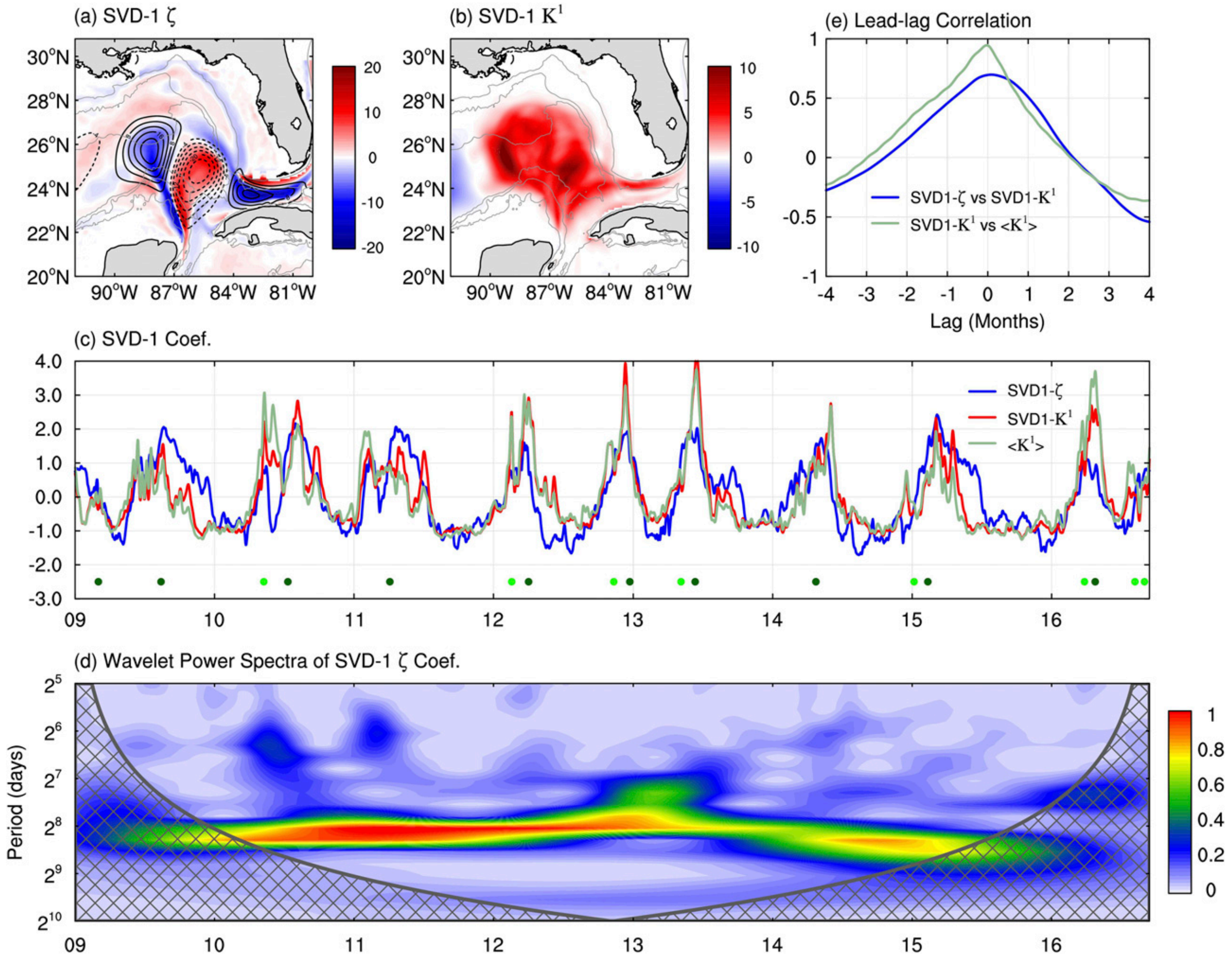

FIG. 7. The spatial patterns for the first SVD mode for the surface (a) total relative vorticity ζ (color shading; $10^{-6}\,\mathrm{s}^{-1}$) and (b) K^1 (color shading; in $10^{-2}\,\mathrm{m}^2\,\mathrm{s}^{-2}$). The black contours in (a) indicate the regression pattern of SSH anomaly (cm) onto the SVD-1 ζ coefficient. (c) Normalized SVD-1 temporal coefficient series for ζ (blue line) and K^1 (red line). The area-mean K^1 (indicated as $\langle K^1 \rangle$) time series averaged over the LC region (see the black-outlined box in Fig. 1) is superimposed (green line). The green dots in (c) indicate the time of eddy detachments in the model, with the dark-green ones marking the final detachments. (d) Rectified wavelet power spectrum for the SVD-1 ζ coefficient. The cross-hatched areas indicate the ''cone of influence'' where edge effects are important. (e) Lead–lag correlations between varies time series. The blue line indicates that the lead–lag correlation between the SVD-1 ζ and K^1 coefficients. A positive lag means that the SVD-1 ζ time series leads the SVD-1 K^1 time series. The green line indicates the lead–lag correlation between the SVD-1 K^1 and $\langle K^1 \rangle$ time series.

mode only captures the LC's dominant variability which is characterized by a train of large-scale SSH anomalies propagating northwestward in the eastern Gulf, while the real shedding is usually determined by the mesoscale eddies or meanders propagating southward on the east side of the LC, which eventually cut through the neck of the LC (see Fig. 3). These two distinct regimes of variabilities are closely coupled. As shown in Fig. 8, the mesoscale EKE level begins to intensify once the LC extends to ~27°N and peaks when the LC's neck is narrowing (due to the growth of the negative SSH anomaly). These results suggest that the extended LC provides a favorable condition for the development of mesoscale EKE, consistent with previous observations (e.g., Donohue et al. 2016; Hamilton et al. 2016). Since the energy of the leading modes peaks mainly within the 200–350 day band (Fig. 7d), a cutoff period of 180 days can efficiently separate them from the variabilities in the mesoscale regime. The resulting fields filtered in this way display reasonable structures associated with their dynamical regimes. For instance, the background flow window successfully captures the LC's low-frequency behavior (see Fig. 3b), similar to the variation of the leading mode as shown in Fig. 8. The mesoscale window is featured with fast-moving meanders (crests and troughs) along the LC front (see Fig. 3c).

The amplitude of these mesoscale signals increases significantly prior to or during the eddy detachment, consistent with the peaks in the EKE time series (Figs. 7d and 8d).

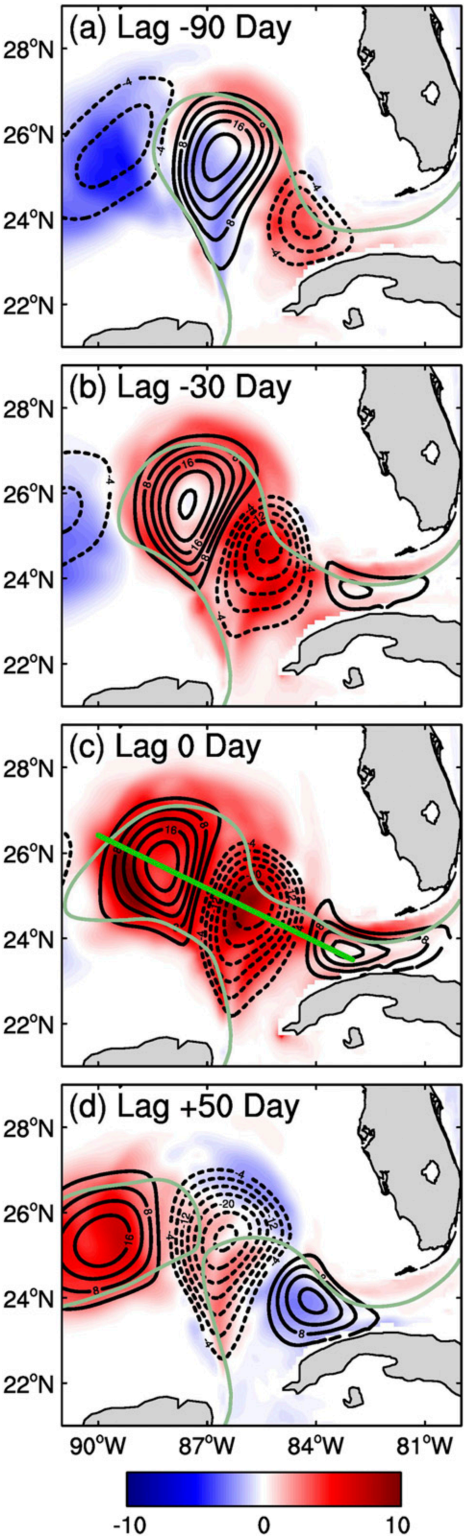

FIG. 8. Lead–lag regressed patterns of the SSH anomaly (black contours; cm) and surface K^1 (color shading; $10^{-2}\,m^2\,s^{-2}$) fields superimposed with the 17-cm contour of the total SSH (green line) at a lag of (a) −90, (b) −30, (c) 0, and (d) +50 days. The regression is based on the SVD-1 K^1 coefficient series. A positive lag means that the SVD-1 K^1 coefficient time series takes the lead. The light-green solid line in (c) denotes the cross section that will be examined in Fig. 9.

6. Mechanisms for the development of EKE associated with the LCE shedding

a. Composite analysis

As explained before, the EKE SVD-1 coefficient time series can be regarded as a reference index of the LCE shedding processes (Fig. 7c). Here, a composite analysis is used to examine the spatial characteristics and differences of the underlying multiscale energetics during both the eddy-shedding (ES) and non-eddy-shedding (nES) phases. The ES phase is defined when the index is greater than +0.8 standard deviation. The nES phase is defined when the index is less than −0.8 standard deviation. The total numbers of days for these ES and nES phases are 579 and 723, respectively. We also tried the criterion as +1 and −1 standard deviation, and the results were almost the same, although with a smaller number of samples (448 and 262 days, respectively). Figures 9a and 9b show the vertical structures of the composite mesoscale EKE (K^1) along a section crossing the eastern deep basin (indicated by the green line in Fig. 8c) during the two phases. The K^1 levels in both the upper and deep layers are enhanced or weakened during the ES phase or nES phase, respectively, consistent with previous studies (Hamilton et al. 2016). Figure 9c displays the time series of volume integrated K^1 in the upper and deep layer (defined as shallower and deeper than 1000 m, respectively). The two time series are highly correlated (correlation coefficient of 0.85), with the upper EKE slightly leading the deep EKE, indicating that the deep-layer dynamics are driven by the upper-layer processes. The time-mean values of the two time series are $2.16 \times 10^{14}\,m^5\,s^{-3}$ and $0.36 \times 10^{14}\,m^5\,s^{-3}$, respectively, although we note that the modeled EKE below 1000 m may be underestimated by a factor of ~2 relative to observations according to Morey et al. (2020). Thus, while the upper-layer drives the lower layer caution should be taken when comparing the relative amplitudes of mesoscale eddy energetics between these layers in the model simulation.

1) UPPER-LAYER ENERGETICS

We first analyze the mesoscale eddy energy budget in the upper layer (i.e., upper 1000 m), and calculate the vertically integrated K^1 budget averaged over the whole simulation period, the ES composite phase, and the nES

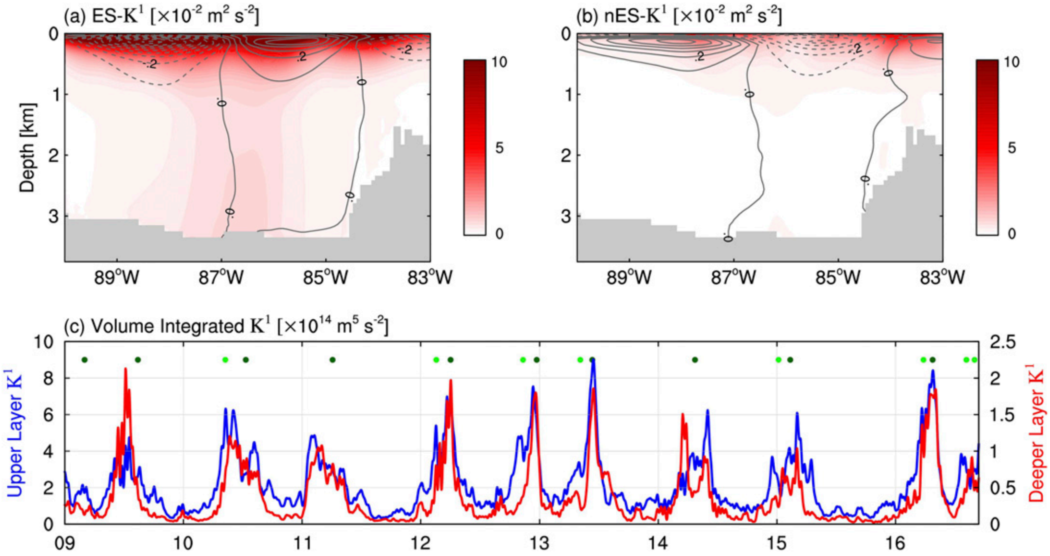

FIG. 9. Composite vertical cross sections of the K^1 (color shading; $10^{-2}\,\mathrm{m^2\,s^{-2}}$) and potential density anomaly (contour; $\mathrm{kg\,m^{-3}}$) in the (a) ES and (b) nES phases.(c) The volume-integrated K^1 time series for the upper layer (blue line) and deep layer (red line).

composite phase (Fig. 10 left, middle and right columns, respectively). The upper K^1 balance in the eastern GoM is mainly dominated by the barotropic canonical transfer $\Gamma_K^{0\to1}$, buoyancy conversion b^1, transport ΔQ_K^1, and horizontal pressure work $\Delta_h Q_P^1$. These energetic processes are enhanced or weakened when the LC is in the ES or nES state, respectively.

The barotropic transfer $\Gamma_K^{0\to1}$ is dominantly positive on the western side of the LC and peaks along the eastern shelf break of the Campeche Bank (black-outlined box in Fig. 10a2). This indicates that the western branch of the LC along the slope is barotropically unstable, resulting in a strong KE transfer from the background flow to the mesoscale perturbations. Comparing the two phases (Figs. 10a2,a3), it is clear that the $\Gamma_K^{0\to1}$ in this region has an increased amplitude during the ES phase, indicating that barotropic instability contributes to the local generation and growth of the mesoscale perturbations along the shelf slope, consistent with previous studies (Chérubin et al. 2006; Garcia-Jove et al. 2016). Another noticeable positive $\Gamma_K^{0\to1}$ center is observed east of the Mississippi Fan during the ES phase. Recall that mesoscale perturbations are frequently formed into coherent cyclonic and anticyclonic eddies (meanders) prior to eddy detachment at this place (see Fig. 3c). This suggests that barotropic instability is an important energy source for the mesoscale variabilities in the upper layer of this region. Interestingly, south of this instability center, a large and strong negative pool of $\Gamma_K^{0\to1}$ is observed, especially during the ES phase. Note that this region is where most of the necking-down of the LC takes place. This indicates that the southward propagating mesoscale meanders (eddies) tend to release their KE back to the background flow when they migrate across the neck of the LC. Negative $\Gamma_K^{0\to1}$ is also seen along the Straits of Florida where the LC exits the GoM. Such eddy-driven variability gets respectively strengthened or weakened during the ES or nES phase (Figs. 10a2,a3).

The three-scale energetics framework enables us to quantify the eddy–eddy interactions between the low-frequency mesoscale and high-frequency frontal eddies. As revealed in Fig. 10b, the eddy–eddy interaction term $\Gamma_K^{2\to1}$ is generally negative, indicating that the high-frequency frontal eddies obtain KE from the lower-frequency mesoscale eddies through a forward energy cascade. Besides, the magnitude of $\Gamma_K^{2\to1}$ is one order of magnitude smaller than $\Gamma_K^{0\to1}$, suggesting that only a small portion of the mesoscale KE is released downscale to smaller scales. These results imply that the high-frequency eddies do not have a significant impact on the mesoscale circulation of the eastern GoM. This is very different from the scenario in the North Pacific western boundary current regions identified in previous studies, where the inverse cascades of KE from high-frequency frontal waves is an important source of intrinsic variability of the mesoscale eddy field (Sérazin et al. 2018; Yang and Liang 2019a). During the ES phase, enhanced negative $\Gamma_K^{2\to1}$ region is located in the deep basin south of the Mississippi Fan (Fig. 10b2), indicating that the forward KE cascades are elevated when the LC sheds an

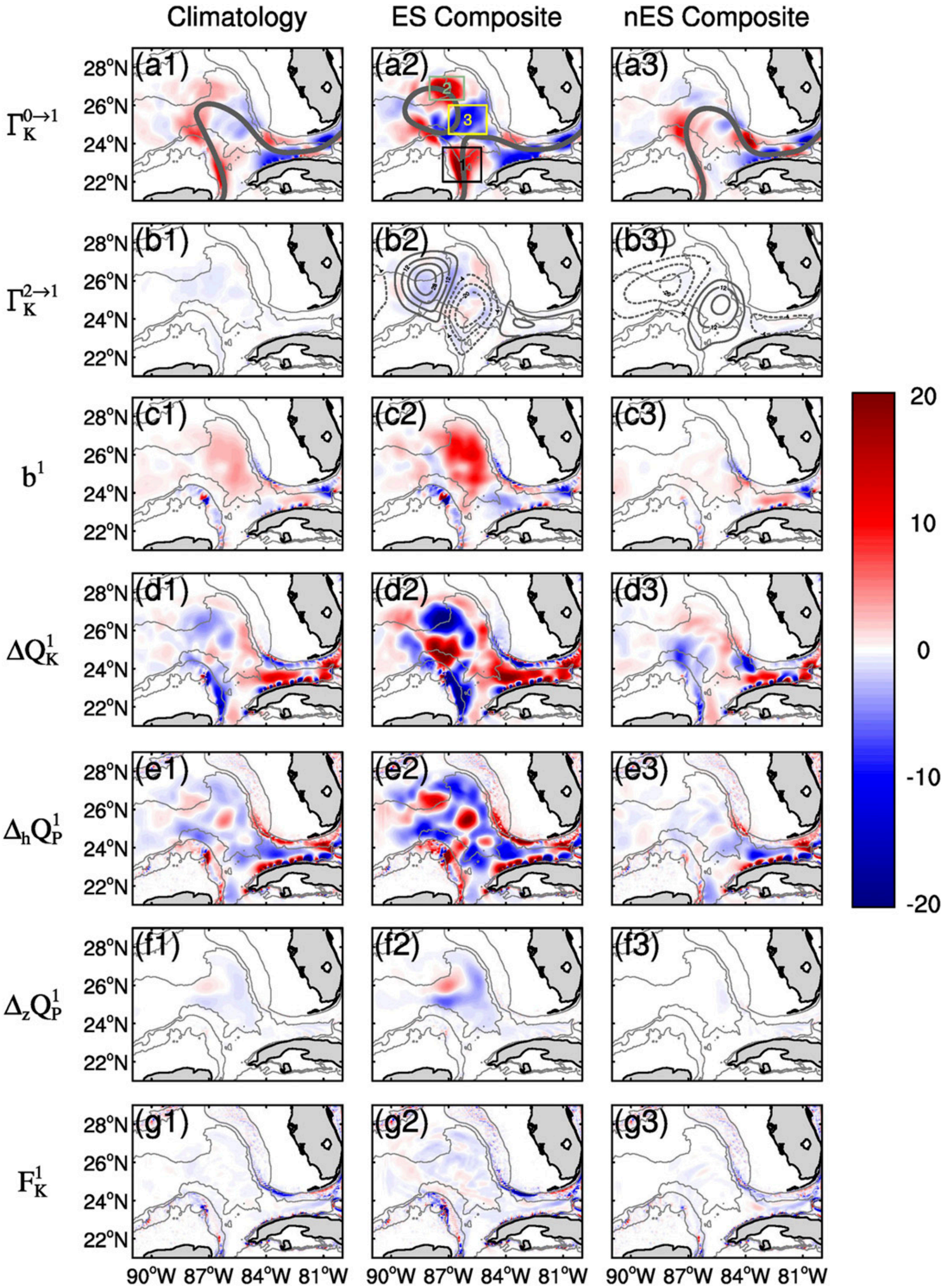

FIG. 10. Horizontal maps of the vertically integrated K^1 energetics (color shading; $10^{-5}\,\mathrm{m^3\,s^{-3}}$) in the upper 1000 m for (left) the long-term climatology, (center) the ES phase composite, and (right) the nES phase composite, showing (a) barotropic transfer from background flow to the mesoscale eddy window $\Gamma_K^{0\to1}$, (b) barotropic transfer from mesoscale to the high-frequency eddy window $\Gamma_K^{2\to1}$, (c) buoyancy conversion rate b^1, (d) advection ΔQ_K^1, (e) horizontal pressure work $\Delta_h Q_P^1$, (f) vertical pressure work $\Delta_z Q_P^1$, and (g) dissipation F_K^1. The 17-cm SSH contour averaged in each state is superimposed (in thick gray) in (a1)–(a3). The SSH anomaly in the ES and nES phases is superimposed in (b2)–(b3). The light-gray contours in (a)–(g) represent the 100-, 1000-, and 3000-m isobaths.

eddy. These results are consistent with Jouanno et al. (2016), who also found no clear connection between the small frontal eddies and the LCE shedding by examining the Hovmöller diagram of the high-pass-filtered SSH along the LC path.

Differing from the other dominant terms in the K^1 equation, the buoyancy conversion rate b^1 shows positive values during the ES phase (Fig. 10c2) over the deep basin region from the base of the west Florida slope to the Mississippi Fan. In contrast, b^1 is almost negligible during the nES phase (Fig. 10c3). These results are consistent with an energy pathway associated with baroclinic instability, which entails the conversion to the EKE from the eddy APE (EAPE).

Based on the in situ data from an array of moored current meters and bottom mounted pressure-recording inverted echo sounders deployed between April 2009 and November 2011, Donohue et al. (2016) showed southward propagation of cyclones and anticyclones in both the upper and deep layers. They diagnosed the EAPE budget equation and identified that the baroclinic instability energy pathway (i.e., $A^0 \rightarrow A^1 \rightarrow K^1$) was established during the LCE separation events. Follow-up studies based on these observations revealed the vertical coupling between the upper and deep layers with the deep eddies leading the upper perturbations as an indication of baroclinic instability (Hamilton et al. 2016, 2019). Note that Donohue et al. (2016) only conducted the EAPE budget analysis; the relative importance of the barotropic and baroclinic instabilities remained unclear.

The nonlocal processes appear in divergence forms in the energy budget equations. In the K^1 budget equation, they are ΔQ_K^1 and ΔQ_P^1, which represent the redistribution of K^1 by advection and pressure work, respectively. The advection term ΔQ_K^1 is negative along the eastern slope of the Campeche Bank and positive in the Straits of Florida (Fig. 10d), indicating that it acts as an energy redistributor that transports EKE from the upstream region where barotropic instability dominates, to the downstream region where inverse KE cascades occur. The strength of the KE transport gets significantly enhanced (weakened) during the ES (nES) phase (Figs. 10d2,d3). It is interesting to note that a strong alternating dipole pattern of ΔQ_K^1 appears in the northern GoM during the ES phase. This feature is related to the southwestward propagation of mesoscale eddies that affect the eddy detachment during this period (Fig. 10d2).

As another nonlocal term within the K^1 budget equation, the horizontal pressure work $\Delta_h Q_P^1$ is dominantly negative in the deep basin of the eastern Gulf (i.e., areas deeper than 1000 m), while positive along the peripheral continental slopes (such as the shelf slopes southwest of the West Florida Shelf, east of the Campeche Bank and north of Cuba; Fig. 10e). That is to say, the pressure work acts to radiate the mesoscale EKE to the surrounding shelf slopes, that otherwise would be accumulated in the deep basin. The largest pressure work is located around the "pressure point" of the West Florida shelf (Liu et al. 2016a), where interactions between the LC and the shelf/slope not only influence the shelf circulation (Hetland et al. 1999; Weisberg and He 2003; Liu et al. 2016a) but may also anchor the LC (Weisberg and Liu 2017). From Fig. 10e2, we see that the pressure work is greatly strengthened in the ES phase to offset the excess eddy energy.

The vertical component of the pressure work $\Delta_z Q_P^1$ integrated in the upper layer is an order of magnitude smaller than its horizontal counterpart (Fig. 10f). Since the vertical components of ΔQ_K^1 and ΔQ_A^1 are negligible (not shown), $\Delta_z Q_P^1$ is the only dominate term in Eq. (18) for exchanging eddy energy between the upper and deep layers. Negative values of $\Delta_z Q_P^1$ occupy the deep basin of the eastern GoM (although mingled with a small area of positive value around 26.5°N, 87°W; see Fig. 10f), indicating that upper-layer mesoscale EKE is transported to the deep layer by pressure work.

The residue F_K^1, which includes all the remaining processes that are not explicitly diagnosed in the current study, reveals overall small and negative values in the eastern GoM (Fig. 10g). This indicates that F_K^1 is mainly dominated by the dissipation processes. The dissipation rate is found to be more prominent along the shelf slopes than in the deep basin, consistent with the previous studies (Moum et al. 2002; Nash et al. 2004). In comparing the two phases, it is seen that the turbulent dissipation near the continental slope seems to be enhanced or weakened during the ES phase or nES phase, respectively.

Diagnosis of the mesoscale EAPE (A^1) budget provides quantitative information on the baroclinic processes in a GFD system (Fig. 11). The upper A^1 budget is dominated by the baroclinic canonical transfer $\Gamma_A^{0\rightarrow 1}$, negative buoyancy conversion $-b^1$, and APE transport ΔQ_A^1. Although mingled with some negative spots (such as at the northeastern tip of the Campeche Bank and the Straits of Florida), the time mean $\Gamma_A^{0\rightarrow 1}$ is mostly positive over the LC region (Fig. 11a1). This means that the LC is overall baroclinically unstable. There is an enhanced APE transfer from the background flow to the mesoscale eddies over the deep basin between the west Florida slope and the Mississippi Fan during the ES phase (Fig. 11a2), indicating that baroclinic instability is an important energy source for the mesoscale eddy

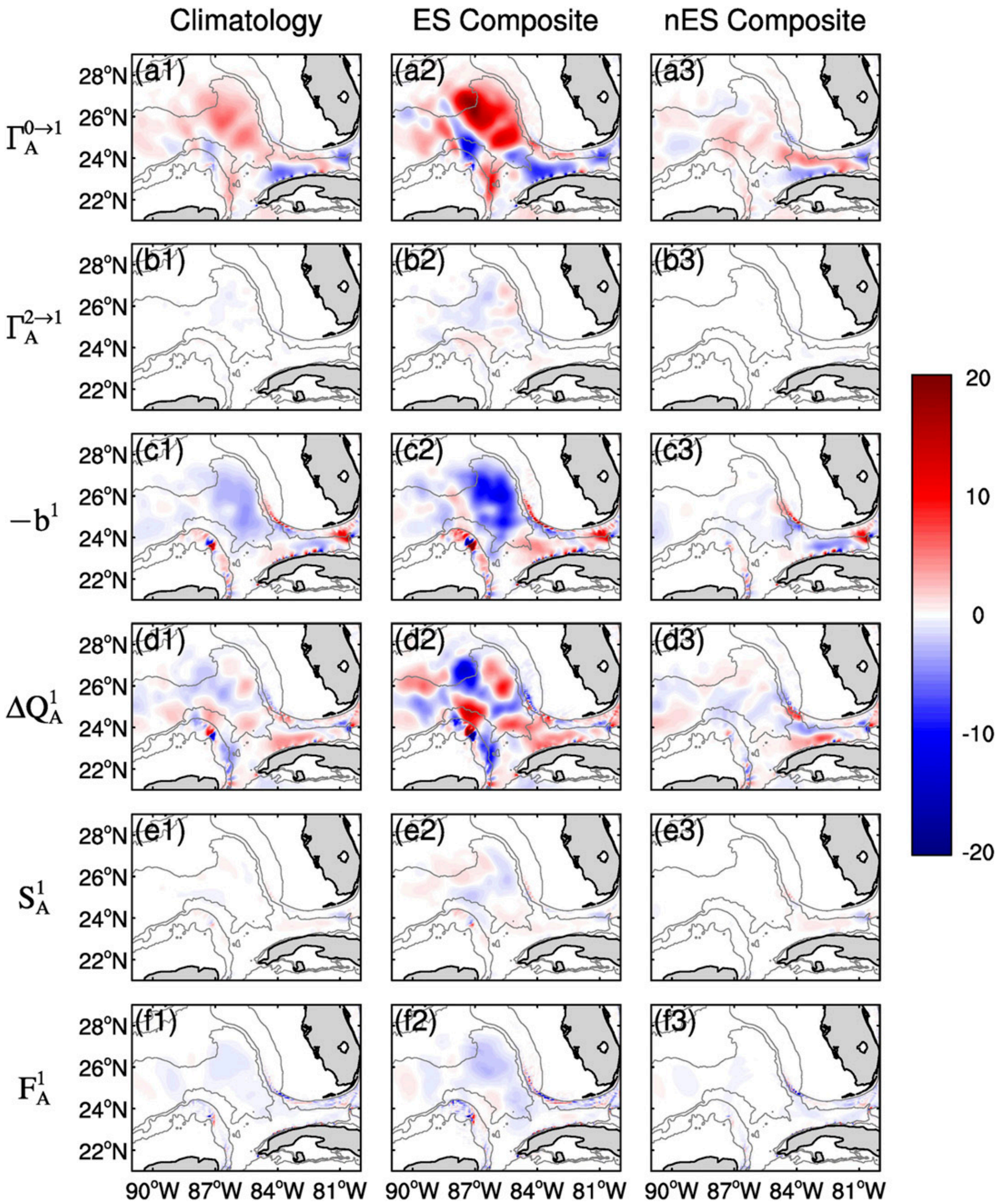

FIG. 11. As in Fig. 10, but for the A^1 energetics integrated through the upper 1000 m: (a) baroclinic transport from background flow to the mesoscale eddy window $\Gamma_A^{0\to1}$, (b) baroclinic transport from mesoscale to the high-frequency eddy window $\Gamma_A^{2\to1}$, (c) buoyancy conversion $-b^1$, (d) APE transport ΔQ_A^1, (e) APE source/sink S_A^1, and (f) APE dissipation F_A^1.

activities in this region. The spatial similarity between the patterns of $\Gamma_A^{0\to1}$ and b^1 during the ES phase (Figs. 11a2, 10c2) indicates the baroclinic instability energy pathway (i.e., $A^0 \to A^1 \to K^1$) during the eddy detachments, in agreement with previous studies (e.g., Donohue et al. 2016). Although elevated positive $\Gamma_A^{0\to1}$ is also observed east of the Campeche Bank along the western branch of the LC during the ES phase, its magnitude is much smaller than its barotropic counterpart $\Gamma_K^{0\to1}$. This implies that EKE production via baroclinic instability is less efficient than barotropic instability at the continental slope. Such a magnitude difference between the two instabilities along the slope of Campeche Bank seems to be consistent with LaCasce et al. (2019) work that a strong slope topography acts to suppress baroclinic instability in favor of barotropic instability in the upper ocean.

It is interesting to note that the canonical baroclinic transfer $\Gamma_A^{0\to1}$ diagnosed from the present MITgcm simulation does not show significant positive values north of the Campeche Bank like the traditional transfer in other models does (Oey 2008; Xu et al. 2013; Garcia-Jove et al. 2016). Such discrepancy could be caused by different behaviors of the LC simulated by different models. Another possible reason could be the different formulations of the cross-scale transfer between the present energetics framework and the classical Lorenz-type formalism. As already shown in section 4, the canonical transfer term in our energetics formalism is rigorously derived, and, most of all, conserves energy in the space of scale [i.e., satisfying the relation in Eq. (15)], which is not met in the classical engineering formalisms. Besides, the suppression phenomenon of baroclinic instability in the presence of slope topography identified in this study seems to be more consistent with previous work (e.g., LaCasce et al. 2019).

Similar to the inverse KE cascades found in the Straits of Florida, a spatially coherent upscale APE transfer from the mesoscale eddy window to the background flow window is also observed in the same region, indicating that the local mean flow draws energy from the eddies to maintain itself. A recent study revealed abundant mesoscale and submesoscale eddies in this region (Zhang et al. 2019). An in-depth investigation of the eddy-driven nature of the LC along the Straits of Florida is worth pursuing in future studies but is beyond the scope of this paper.

The APE transport ΔQ_A^1 is one of the three dominant terms in the A^1 budget equation. Similar to its counterpart in the K^1 equation, this term serves to redistribute the A^1 gained from A^0 via baroclinic instability, and its intensity respectively increases or decreases during the ES phase or nES phase (Fig. 11d). The $\Gamma_A^{2\to1}$ and S_A^1 are an order-of-magnitude smaller than the dominant terms (Figs. 11b,e).

By hydrodynamic instability theory, a necessary condition for barotropic instability is that the cross-stream gradient of potential vorticity (PV) must change sign, while for the occurrence of baroclinic instability, a necessary condition is that the cross-stream gradient of PV must change sign with depth (Pedlosky 1987). The Ertel PV Q in the ocean can be written as

$$Q = -\frac{1}{\rho_0}(2\boldsymbol{\Omega} + \nabla \times \mathbf{v}) \cdot \nabla \rho_\theta, \qquad (19)$$

where $2\boldsymbol{\Omega}$ is the vector of Earth's rotation velocity and ρ_θ is the potential density (Ertel 1942). To examine whether the abovementioned canonical transfers are consistent with the classical instability theorems, we plot the cross gradients Q_x at two transections perpendicular to the time-mean LC axis (Figs. 12a,d). The first section is located at the west branch of LC over the upper shelf slope region of the Campeche Bank (the blue dashed line in Fig. 1), and the second one is at the east branch of the LC (the red dashed line in Fig. 1). The sign of Q_x is changed cross stream (Fig. 12a), suggesting that the western branch of LC meets the necessary condition for barotropic instability. Vertical changes in the sign of Q_x are also pronounced in the upper 500 m over the continental slope, indicating possibility for baroclinic instability to occur. These results agree with the positive barotropic and baroclinic canonical transfers as revealed in Figs. 12b,c. Different from section 1, the cross-stream changes in sign of Q_x are not evident in section 2 where the eastern branch of the LC flow over the deep basin (Fig. 12d). In contrast, the vertical sign reversal is pronounced in this region (Fig. 12d). This means that the LC at this region meets the necessary condition for baroclinic instability but not for barotropic instability, agreeing with the large positive $\Gamma_K^{0\to1}$ and negative $\Gamma_K^{0\to1}$ as revealed in Figs. 12e,f. Here we remark that the above conditions are just necessary conditions for instabilities; they are not sufficient. The time-dependent nature of instabilities and the relative contributions to local eddy formation made by these instabilities can be revealed by the canonical transfers.

In summary, we present a quantitative discussion of the upper-layer eddy energetics. Table 1 summarizes the mesoscale eddy kinetic and potential energy budgets of the long-term mean, ES and nES phase in a volume-integrated way. The volume integration is taken over the whole LC region (see the black box in Fig. 1) and the upper 1000-m vertical water column. Over the long-term mean, the $\Gamma_K^{0\to1}$ and b^1 are the two dominant sources of K^1 in this region, which accounts for 57% and 43% of the total K^1 sources, respectively. The ΔQ_P^1, ΔQ_K^1, F_K^1, and $\Gamma_K^{2\to1}$ are sinks for the upper K^1, which accounts for 41%, 34%, 14%, and 11% of the total K^1 sinks, respectively. Particularly, about 11% of the upper-layer K^1 sinks go to the deeper layer via vertical pressure work $\Delta_z Q_P^1$. Regarding the upper-layer volume-integrated A^1 budget, the baroclinic transfer $\Gamma_A^{0\to1}$ is the major source of A^1 (account for more than 99% of the total A^1 sources), while the forward APE cascade to frontal-scale eddies $\Gamma_A^{2\to1}$, buoyancy conversion to EKE $-b^1$, advection ΔQ_A^1, and dissipation F_A^1 are the mechanisms that damp the A^1 in this region (accounting for 6%, 59%, 15%, and 20% of the total A^1 sinks, respectively). With regard to the differences in these energetics between the two opposite phases, the volume-integrated baroclinic transfer in the ES phase is 4.2 times as strong as that in the nES phase. In contrast, the integrated barotropic transfer does not differ much between the two phases; it is even smaller during the ES

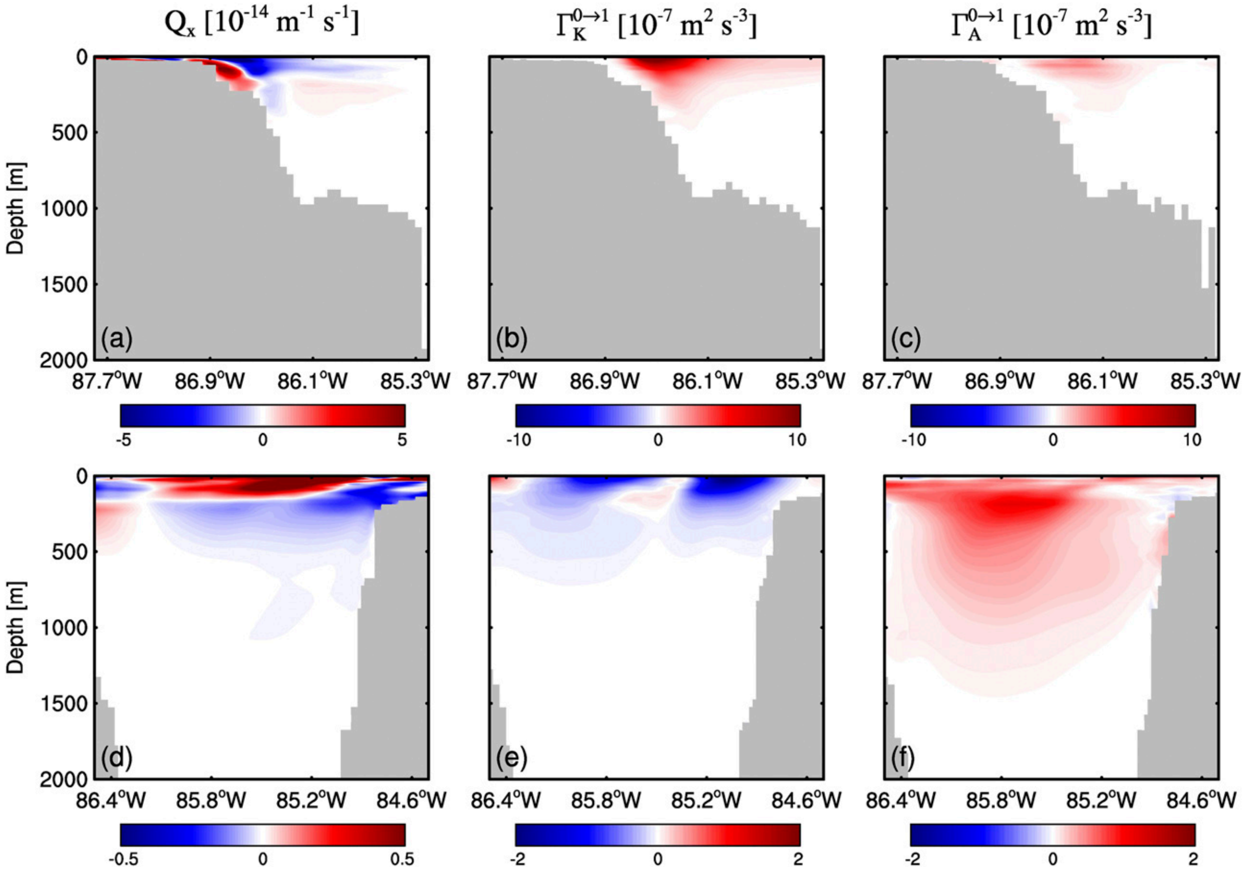

FIG. 12. The vertical structures of (a),(d) cross-stream gradient of Ertel PV Q_x (10^{-14} m^{-1} s^{-1}), (b),(e) $\Gamma_K^{0\to1}$ (10^{-7} m^2 s^{-3}), and (c),(f) $\Gamma_A^{0\to1}$ (10^{-7} m^2 s^{-3}) for (top) section 1 (indicated by the blue dashed line in Fig. 1) and (bottom) section 2 (indicated by the red dashed line in Fig. 1).

phase comparing to the nES phase which is not surprising due to the offset of strong positive and negative values as can be seen from ES composited map (Fig. 10a2). Also notice that the mesoscale eddy-frontal-scale eddy interaction is in a forward-cascade sense in the LC region; the forward KE cascade is enhanced when there are more mesoscale eddies in the basin. This indicates that the high-frequency frontal eddies are fed by the mesoscale eddies in this region. [The relative contributions of transfers to these high-frequency frontal eddies from the background LC and the mesoscale eddies is another topic of interest with a focus on the high-frequency eddy window ($\varpi = 2$); here we leave it to future studies]. The excess mesoscale eddy energy generated during the ES phase in the upper layer has to be balanced. This is fulfilled by elevated levels of offset mechanisms such as the outgoing energy advection, horizontal and vertical radiation by pressure work, forward cascades to frontal eddies, and internal dissipations.

2) DEEP-LAYER ENERGETICS

As a part of the LC system, the deep-layer (below 1000 m) variabilities also play a role in the LCE shedding process (Oey 2008; Chang and Oey 2011; Xu et al. 2013; Donohue et al. 2016; Hamilton et al. 2016, 2019).

TABLE 1. Energetics (10^6 m^5 s^{-3}) integrated over the upper-layer LC region (indicated by the black box in Fig. 1) for the long-term mean, ES, and nES composited phases.

	$\Gamma_K^{0\to1}$	$\Gamma_K^{2\to1}$	b^1	ΔQ_K^1	$\Delta_h Q_P^1$	$\Delta_z Q_P^1$	F_K^1	$\Gamma_A^{0\to1}$	$\Gamma_A^{2\to1}$	ΔQ_A^1	S_A^1	F_A^1
Mean	14.30	−2.66	10.67	−8.51	−7.55	−2.75	−3.50	18.25	−1.11	−2.73	0.04	−3.73
ES	12.85	−5.50	23.43	−10.04	−10.63	−6.29	−5.67	33.59	−0.57	−1.69	−0.39	−6.86
nES	15.08	−1.43	2.43	−7.54	−4.57	−0.85	−2.51	7.96	−0.78	−2.45	0.46	−1.99

In section 3, we showed that the deep mesoscale eddies tend to be jointly intensified with their upper-layer counterparts prior to and during the shedding (Fig. 3). A natural question is what are the processes involved in the generation and growth of these deep eddies. To answer this, we analyze the eddy energetics of the deep layer.

Before investigating the energetics, we first examine the spatial patterns of the deep circulation when averaged over the whole simulation period and over the composite ES and nES phases (Fig. 13a). The long-term mean velocity vector map reveals an anticyclone–cyclone pair underneath the mean LC (Fig. 13a1), consistent with observations (Pérez-Brunius et al. 2018; Hamilton et al. 2019). During the ES phase, a well-defined cyclonic gyre is established in the eastern basin (Fig. 13a2), which is also consistent with previous studies (Chang and Oey 2011; Xu et al. 2013). Chang and Oey (2011) showed that the westward-extended LC forces a deep return flow from the western into the eastern Gulf and therefore a convergence beneath the LC, generating cyclonic relative vorticity according to PV conservation. During the nES phase, in contrast, the deep circulation is characterized by an anticyclonic gyre (Fig. 13a3). The above results give us confidence that the deep-layer dynamics is reasonably captured by the model. However, as mentioned previously, the variance of the deep circulation may be underestimated by the model when compared to observations.

Figure 13 shows the horizontal patterns of the K^1 budget terms integrated over the deep layer. Weak barotropic canonical transfer from the mesoscale window to the background flow window (i.e., negative $\Gamma_K^{0\to 1}$) is observed inside the deep cyclonic gyre during the ES phase (Fig. 13a2), indicating that barotropic instability is not an energy source for deep eddies. In contrast, positive regions of b^1 and $\Gamma_A^{0\to 1}$ residing inside the cyclonic gyre during ES phase indicates that the baroclinic energy pathway (i.e., $A^0\to A^1\to K^1$) is well established in the deep layer during eddy shedding (Figs. 13b2, 14a2), consistent with previous studies (Donohue et al. 2016; Hamilton et al. 2016). The vertical component of pressure work ($\Delta_z Q_P^1$) in this layer exhibits dominantly positive value in the deep eastern basin, especially in the ES phase, which is of opposite sign to that integrated in the upper layer (see Figs. 10f and 13e). (The almost cancelling between the vertical pressure work integrated in the upper and lower layers suggests that the vertical pressure fluxes at the surface and the bottom are negligible.) This suggests that the downward energy radiation from the upper layer serves as an important source of the deep EKE. Recall that the mesoscale eddy energy generation is mainly confined in the upper layer (see Fig. 12), and the downward pressure flux acts as a conduit to couple the eddy energy between the upper and lower layers. Similar processes are also found in the North Atlantic subtropical gyre (Zhai and Marshall 2013). The horizontal component of pressure work displays a rather chaotic pattern in the deep layer, which is generally negative inside the deep basin and positive at the boundary of the deep basin (Fig. 13d). Very different from the upper layer, the damping of the deep eddy energy is mainly fulfilled by the residual term F_K^1, which is sensible by the virtue of bottom drag. From Fig. 13f, one can see that the strength of dissipation is greatly enhanced during the ES phase.

Table 2 summarizes the mesoscale eddy energy route in the deep layer. The vertical pressure work and baroclinic canonical transfer are the dominant eddy mechanical energy sources in this layer. They are 12.8 and 9.3 times larger in magnitudes during the ES phase than the nES phase, respectively. Note that the conversion $A^1\to K^1$ (i.e., b^1) is nearly zero during the nES phase, suggesting that the baroclinic instability pathway in the deep layer is largely suppressed when no shedding occurs. The excess deep EKE is damped by dissipation, horizontal radiation by pressure work, inverse cascade to background flow (negative $\Gamma_K^{0\to 1}$), and forward cascade to high-frequency motions (negative $\Gamma_K^{2\to 1}$), which account for 82%, 11%, 3.5%, and 3.5% of the total EKE sinks during the ES phase.

b. Temporal variation

In the previous section we gave a detailed description of the spatial structures of the mesoscale eddy energetics from a composite point of view. Here we further extend the analysis to a time-dependent perspective by taking advantage of the localized nature of MWT. Figure 15 shows the time series of some relevant energy terms integrated over the same upper-layer volume as that in Table 1. Note that all these data are original daily time series without any low-pass filtering. The integrated barotropic canonical transfer $\Gamma_K^{0\to 1}$ is found not well correlated with the EKE in the upper layer (Fig. 15a) due to the cancelling of the positive and negative values in the considered domain. Three subdomains (marked as box 1–3 in Fig. 10a2) are further selected to investigate the regional instability property of the LC. Lead–lag correlation analysis shows that $\Gamma_K^{0\to 1}$ in box 1 and 2 are positively correlated with regional EKE with correlation coefficients of 0.51 and 0.55 (statistically significant at the 95% confidence level), respectively, when the $\Gamma_K^{0\to 1}$ takes a lead for a few days. This demonstrates that barotropic instability is responsible for the generation/intensification of the mesoscale eddies around the eastern shelf break

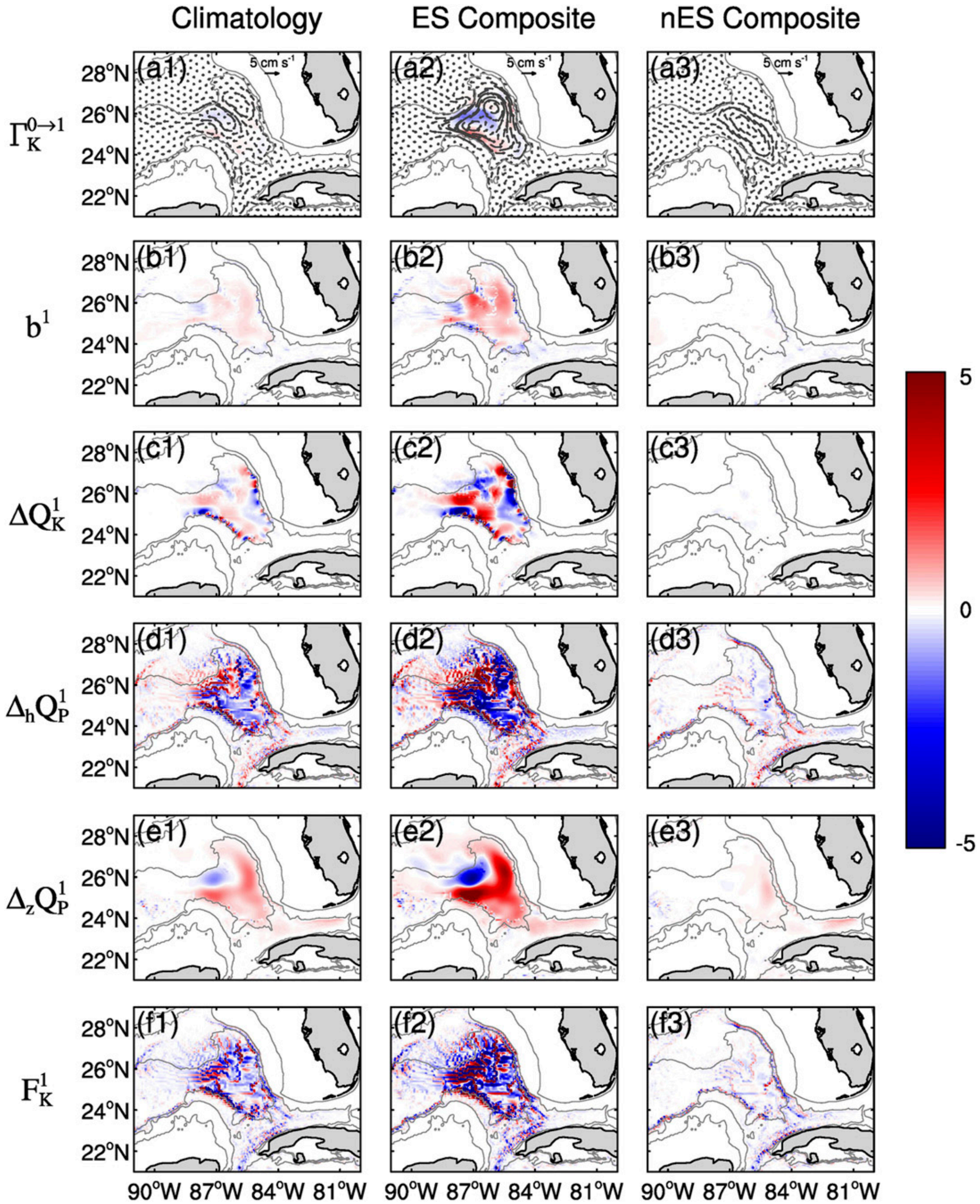

FIG. 13. As in Fig. 10, but for the K^1 energetics integrated from bottom to 1000 m. The deep-layer depth-averaged velocity in each state is superimposed in (a) (in gray vectors).

of the Campeche Bank (box 1) and a small region east of the Mississippi Fan (box 2). On the contrary, the $\Gamma_K^{0\to1}$ and EKE in box 3 are negatively correlated with no apparent lag, suggesting the mesoscale eddies immediately feed back to the background flow through inverse KE cascade. The baroclinic transfer and buoyancy conversion integrated over the entire LC region are significantly correlated with the EKE time series (Figs. 15b,c). A closer look at the lead–lag relations in the three small subdomains as mentioned above, we find that the baroclinic instability is not well established in box 1, that is, along the shelf break east of Campeche Bank, consistent with previous finding that baroclinic instability could be sufficiently suppressed over continental slopes (LaCasce et al. 2019). The above time-varying energetics results suggest that the major energy source for the eddy growth during the shedding is distinct on the west and east side of the LC. Barotropic instability mainly contributes to the

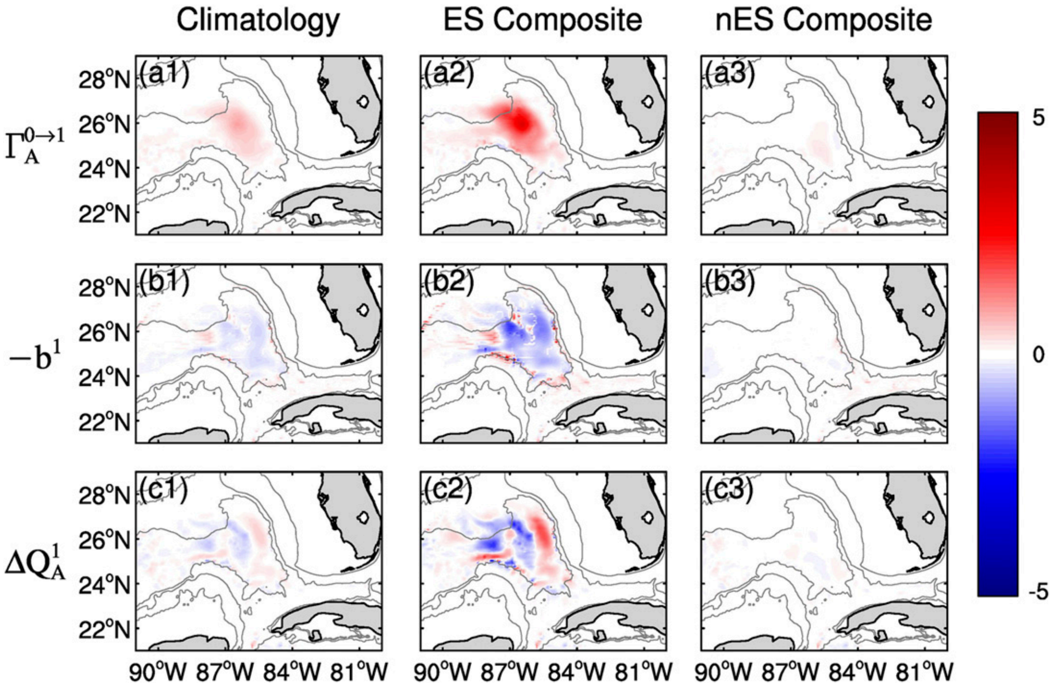

FIG. 14. As in Fig. 11, but for the A^1 energetics (only the three dominant terms are shown) integrated from bottom to 1000 m.

generation/intensification of the mesoscale eddies over the eastern continental slope of the Campeche Bank. These eddies propagate along the LC front and experience their second major growth (much more intense than the first growth along the slope) along the eastern side of the LC due to baroclinic instability, and eventually cause the LCE shedding by cutting through the neck of the LC (e.g., Schmitz 2005).

Figures 15d and 15e show the time series of the volume-integrated ΔQ_K^1 and $\Delta_h Q_P^1$ in the upper layer, respectively. These two processes are negatively correlated with EKE, indicating that the EKE produced by the two instabilities is mainly damped by nonlocal processes via advection and pressure work. Finally, the significant negative correlation between the $\Delta_z Q_P^1$ and EKE demonstrate that a portion of the upper-layer EKE is radiated into the deep layer via pressure work.

The time series of the eddy energy budget terms and their relations with EKE in the deep layer are provided in Fig. 16. It can be seen that $\Delta_z Q_P^1$ is almost in phase with the deep EKE (Fig. 16e; correlation coefficient reaches 0.81 when $\Delta_z Q_P^1$ leads K^1 by ~10 days), indicating that the EKE is generated in the upper layer, and it is radiated downward to the deep layer by pressure work. The baroclinic instability in the deep layer is also found to be in phase with the deep EKE, although with a smaller amplitude compared to $\Delta_z Q_P^1$ (Figs. 16b,c). As we mentioned before, the deep EKE is significantly underestimated compared to observations, due to a weaker deep water baroclinic instability in the model, or a weaker upper–lower-layer coupling through $\Delta_z Q_P^1$, or both. The relative importance of the above two mechanisms for generating deep eddies needs to be verified with observations. The deep mesoscale eddy energy gained from the above two mechanisms is mostly damped by dissipation processes (Fig. 16f).

To further illustrate the nature of the mesoscale eddy energy sources and sinks in the LC region, we plot the cumulative time series of the volume-integrated mechanical budget [Eq. (18)] in Fig. 17. For the upper layer,

TABLE 2. As in Table 1, but for the deep-layer energetics.

	$\Gamma_K^{0\to1}$	$\Gamma_K^{2\to1}$	b^1	ΔQ_K^1	$\Delta_h Q_P^1$	$\Delta_z Q_P^1$	F_K^1	$\Gamma_A^{0\to1}$	$\Gamma_A^{2\to1}$	ΔQ_A^1	S_A^1	F_A^1
Mean	−0.06	−0.11	0.63	0.09	−0.31	2.80	−3.03	1.56	−0.20	−0.08	−0.15	−0.52
ES	−0.29	−0.29	1.79	0.12	−0.93	6.51	−6.83	3.64	−0.44	−0.10	−0.37	−1.02
nES	0.01	−0.00	0.00	0.01	−0.03	0.81	−0.73	0.39	−0.03	−0.02	−0.02	−0.15

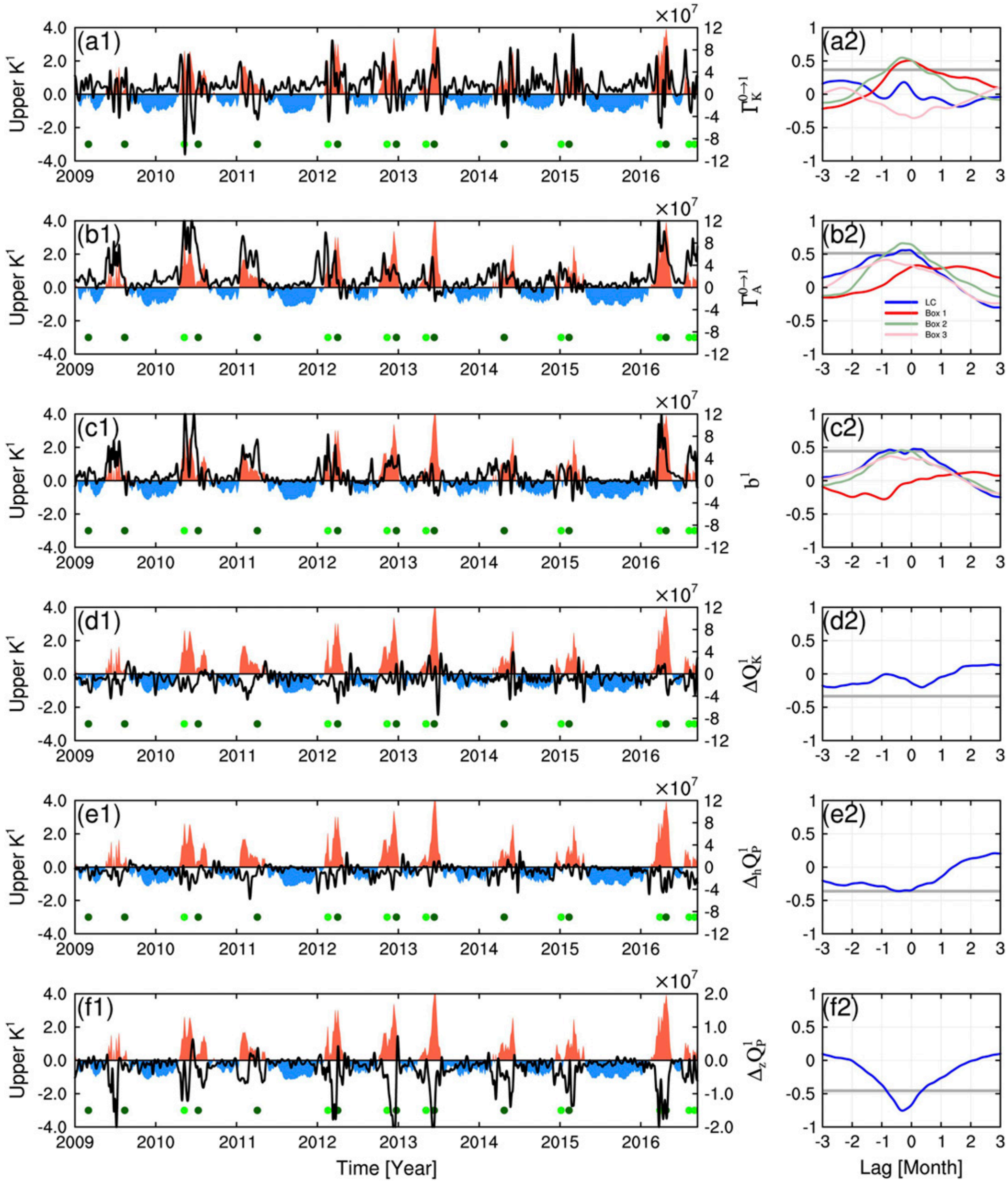

FIG. 15. (a1) Daily time series of the normalized upper-layer integrated mesoscale EKE (K^1, red and blue bars; same as the red line in Fig. 9c except that here the time series is normalized) and kinetic energy transfer from background flow to the mesoscale eddy window ($\Gamma_K^{0\to1}$; black line; $10^7\ \mathrm{m^5\,s^{-3}}$) integrated over the entire LC region (see the black-outlined box in Fig. 1). The green dots are the same as in Fig. 2. (a2) Lead–lag correlation between these two time series (blue line). A positive lag means that K^1 leads $\Gamma_K^{0\to1}$. The thick gray line indicates the 95% confidence level. (b)–(g) As in (a), but for $\Gamma_A^{0\to1}$, buoyancy conversion rate b^1, advection ΔQ_K^1, horizontal pressure work $\Delta_h Q_P^1$, and vertical pressure work $\Delta_z Q_P^1$ respectively. Note that the color scale is decreased for $\Delta_z Q_P^1$ in (f1). The red, green, and pink lines in (a2) indicate lead–lag correlations between $\Gamma_K^{0\to1}$ and K^1 averaged over the three small domains (marked as boxes 1–3 in Fig. 10a2), respectively. The red, green, and pink lines in (b2) and (c2) are as in (a2), but for correlations between $\Gamma_A^{0\to1}$ and K^1 and correlations between b^1 and K^1, respectively.

baroclinic instability accounts for most of the production of eddy mechanical energy through APE transfer from the background flow to the eddies (Fig. 17a). Barotropic instability is also a source but its contribution is about 22% smaller than baroclinic instability. The eddy energy gained via the above two instability processes is mainly balanced by the two divergence terms, that is, ΔQ_E^1 and $\Delta_h Q_P^1$. The relative magnitude of these two

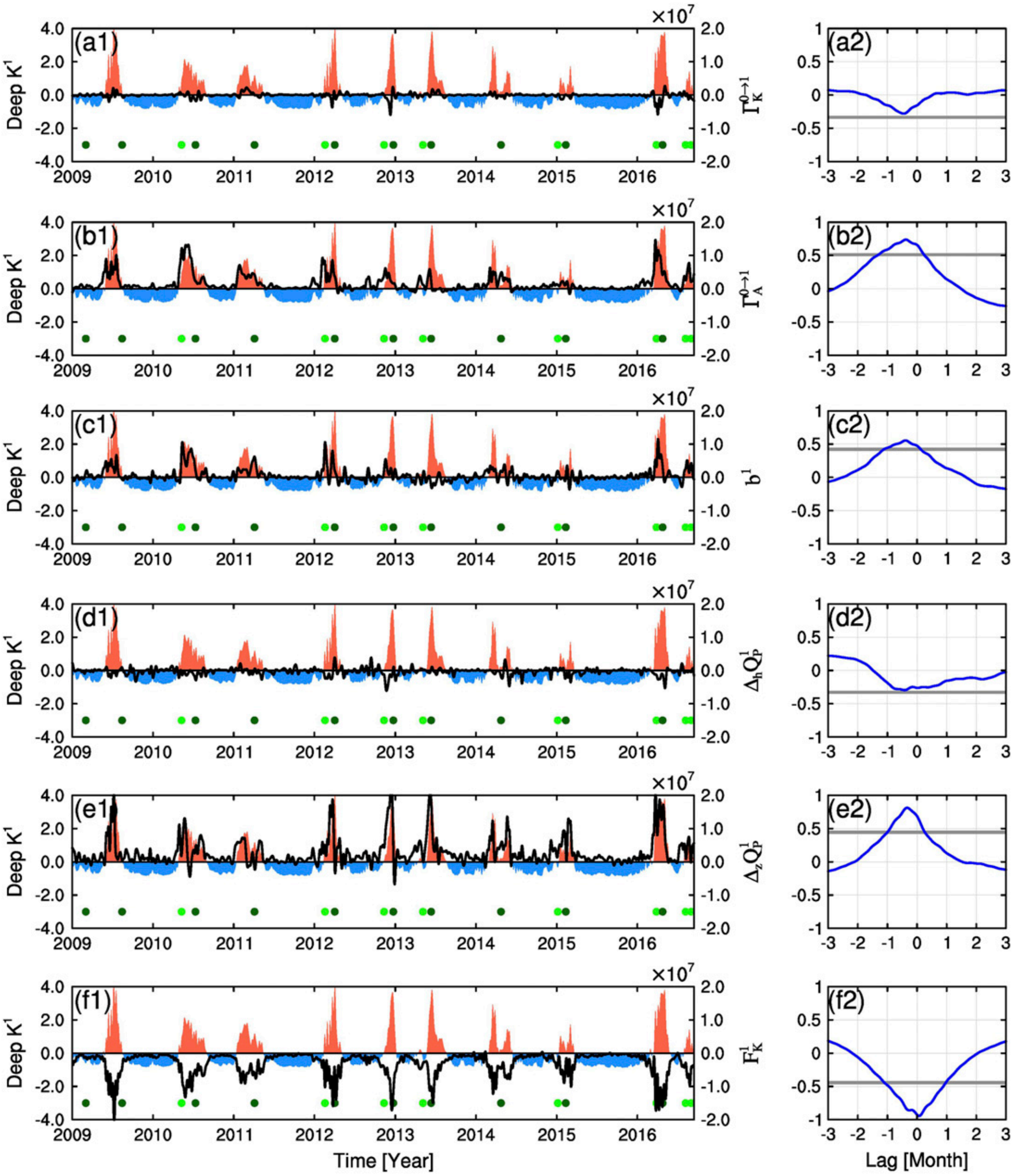

FIG. 16. As in Fig. 15, but for the deep layer.

nonlocal processes is sensitive to the selection of the integration domain. For example, if we only consider the volume integration in the deep basin, the pressure work will become a dominant mechanism to consume the eddy energy (Fig. 17b). Apart from the above-mentioned nonlocal processes, the mesoscale energy is also taken by local processes such as forward cascades to smaller scales $\Gamma_E^{2\to1}$, vertical energy transport to the lower layers $\Delta_z Q_P^1$ and other dissipation processes F_E^1. Note that the contributions to upper-layer eddy energy consumption from $\Gamma_E^{2\to1}$ and $\Delta_z Q_P^1$ in the considered region are comparable, indicating that the forward cascades to high-frequency frontal motions is an important energy sink of the mesoscale eddy energy budget in this layer.

With regard to the deep layer (Fig. 17c), the downward energy transport account for most of the eddy energy source through vertical pressure work. Baroclinic instability also serves as a source but is 44% smaller than the vertical pressure work. Again, we see that the deep eddy energy is predominantly damped by dissipation processes. When integrated throughout the whole water column (Fig. 17d), the relative contribution of baroclinic and barotropic instability as eddy energy source

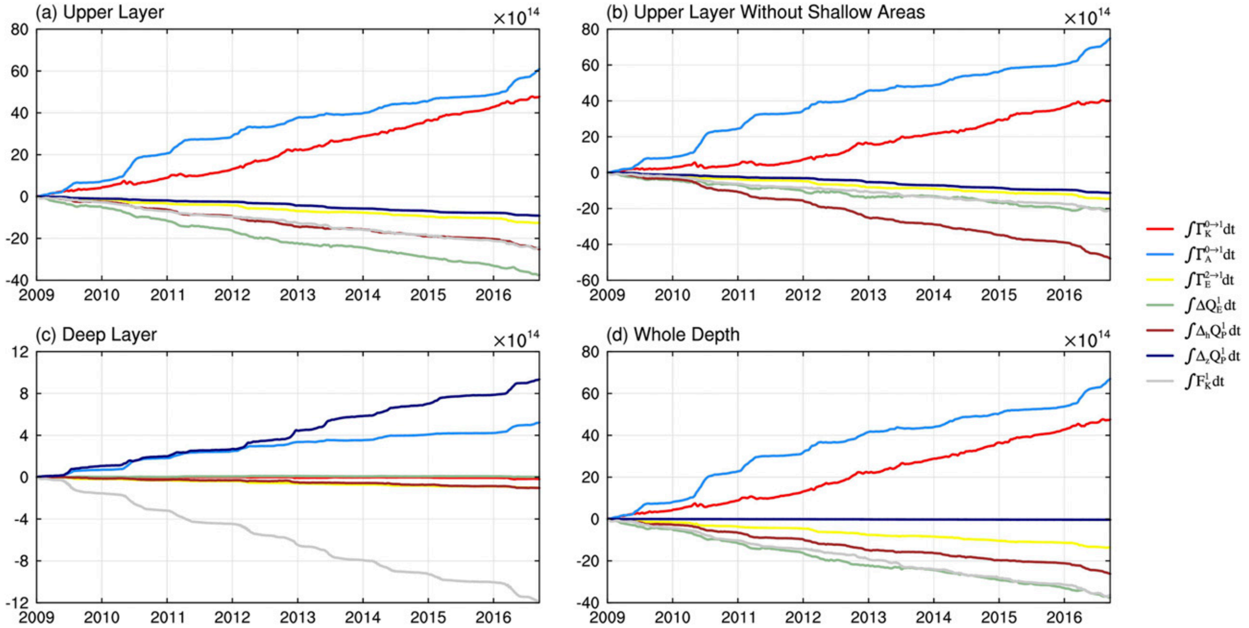

FIG. 17. (a) Cumulative budget of the upper-layer (0–1000 m) mesoscale mechanical energy (10^{14} m^5 s^{-2}) integrated over the box as indicated in Fig. 1. Each term corresponds to the time-integrated versions of those in the mechanical energy budget [Eq. (18)]: barotropic and baroclinic transfers from background flow to the mesoscale eddy window ($\Gamma_K^{0\to1}$, $\Gamma_A^{0\to1}$), transfer from mesoscale to the high-frequency eddy window $\Gamma_E^{2\to1}$, advection ΔQ_E^1, horizontal pressure work $\Delta_h Q_P^1$, vertical pressure work $\Delta_z Q_P^1$, and dissipation F_E^1. (b) As in (a) except that the coastal areas with depth shallower than 1000 m are not included in the volume integration. (c),(d) As in (a), but for the budget integrated in the deep layer (below 1000 m) and throughout the entire depth, respectively.

resembles that integrated in the upper layer. As for the sink terms, the advection ΔQ_E^1 and dissipation F_E^1 are the two leading mechanisms, followed by the pressure work and forward cascades to smaller scales.

7. Summary

As one of the most fascinating phenomena in physical oceanography, the LCE shedding in the GoM has been an important area of research for decades (National Academies of Sciences Engineering and Medicine 2018). In this study, a three-scale energetics framework is employed to investigate the multiscale interaction processes underlying the LCE shedding, based on a high-resolution regional model (free run) simulation. The original fields are decomposed into a background flow window (periods >180 days), a mesoscale eddy window (20–180-day periods), and a high-frequency frontal eddy window (periods <20 days). The background flow window includes the cycle of wax and wane of the LC (dominant periods around 200–350 days), which is manifested as a northwestward propagating train of large-scale SSH anomaly centers of alternating signs in the eastern basin. The mesoscale window captures low-frequency, mesoscale eddies moving along the axis of the LC jet. When the LC extends into the eastern basin, these mesoscale eddies begin to grow and propagate southward along the eastern branch of the LC and eventually affect the eddy shedding by cutting through the neck of LC. Such coupling between the background LC and the mesoscale eddies is confirmed by applying a singular value decomposition (SVD) analysis of the surface relative vorticity and mesoscale EKE in the eastern Gulf. The high-frequency eddy window is characterized by small-scale wavelike motions that propagate along the periphery of the LC.

By diagnosing the canonical transfers between the background flow and the mesoscale eddies in the upper layer, it is found that the major energy sources for the eddy growth during the shedding event are distinctly different on the western and eastern sides of the LC. Barotropic instability mainly contributes to the initial generation/intensification of the eddies over the eastern continental slope of the Campeche Bank where baroclinic instability is suppressed due to the slope topography. These eddies propagate along the LC front and experience another major growth interval (more intense than the first one) along the eastern branch of the LC in the deep basin between the west Florida slope and the Mississippi Fan. The second growth interval is by baroclinic instability, consistent with previous observational studies (Donohue et al. 2016; Hamilton et al. 2016). The growth of these mesoscale eddies may eventually cause the LCE shedding by cutting through the neck of the LC (e.g., Schmitz 2005). The barotropic canonical transfer map also shows that the eddies tend to lose their KE back to the background LC through strong inverse cascade processes in the neck-down region. The three-scale energetics analysis also reveals that the mechanical energy transfer between the mesoscale eddies and the high-frequency frontal eddies is only a small component in the mesoscale eddy energy budget, generally in a downscale sense; that is, this scale interaction acts to damp rather than strengthen the mesoscale eddies.

For the deep layer, the leading source of eddy energy is from the upper layer by vertical pressure work. Baroclinic instability also releases energy to support the deep eddy development during the LCE shedding, while barotropic instability is negligible in this layer. A budget analysis shows that the mesoscale eddy energy generated through the two instabilities is mainly balanced by horizontal advection, pressure work and dissipation.

The two-pronged mechanism of barotropic instability initiating the mesoscale eddies along the Campeche Bank shelf slope, followed by baroclinic instability adding to this farther to the northeast in deeper water, is not unlike instabilities found elsewhere. An example is provided by the tropical instability waves of the equatorial Atlantic and Pacific Oceans wherein barotropic instability provides the initiating mechanism in the vicinity of the equator (e.g., Weisberg and Weingartner 1988; Yu et al. 1995; Qiao and Weisberg 1998) with baroclinic instability adding to this at latitudes farther north (e.g., Cox 1980; Masina et al. 1999).

Last, whereas the onset of tropical instability waves follows a regular seasonal intensification of the equatorial current system, the instabilities associated with LC eddy shedding appear to be of a more intrinsic nature. So while the mechanics of the LCE shedding are further revealed by this numerical model study, the ability to predict the occurrence of instability resulting in LCE shedding remains elusive.

Acknowledgments. The authors thank Julio Sheinbaum, an anonymous referee, and the editor for constructive comments. The data used in this study are available online (http://www.ecco.ucsd.edu/gom.html). Author Yang thanks Ganesh Gopalakrishnan for helping to access the data. Yang and author Liang are supported by the National Science Foundation of China (NSFC) under Grants 41806023 and 41975064, 2015 Jiangsu Program of Entrepreneurship and Innovation Group, NUIST Startup Program (2017r054), Natural Science Foundation of the Higher Education Institutions of Jiangsu Province (18KJB170019), and the CSC–SOA Joint Scholarship Program (201804180031). Authors Weisberg and Liu are partially supported by the National Academies of Sciences, Engineering and Medicine (NASEM) UGOS-1 (2000009918), the Gulf of Mexico Research Initiative (GoMRI) (G-231804), and the NOAA IOOS SECOORA Program (NA16NOS0120028). Data are publicly available through the Gulf of Mexico Research Initiative Information and Data Cooperative (GRIIDC; https://data.gulfresearchinitiative.org/pelagos-symfony/data/R6.x820.000:0008) (doi:10.7266/0W5RFXFM).

REFERENCES

Alvera-Azcárate, A., A. Barth, and R. H. Weisberg, 2009: The surface circulation of the Caribbean Sea and the Gulf of Mexico as inferred from satellite altimetry. *J. Phys. Oceanogr.*, **39**, 640–657, https://doi.org/10.1175/2008JPO3765.1.

Androulidakis, Y. S., V. H. Kourafalou, and M. Le Hénaff, 2014: Influence of frontal cyclone evolution on the 2009 (Ekman) and 2010 (Franklin) Loop Current eddy detachment events. *Ocean Sci.*, **10**, 947–965, https://doi.org/10.5194/os-10-947-2014.

Athié, G., J. Candela, J. Ochoa, and J. Sheinbaum, 2012: Impact of Caribbean cyclones on the detachment of Loop Current anticyclones. *J. Geophys. Res.*, **117**, C03018, https://doi.org/10.1029/2011JC007090.

Bretherton, C. S., C. Smith, and J. M. Wallace, 1992: An intercomparison of methods for finding coupled patterns in climate data. *J. Climate*, **5**, 541–560, https://doi.org/10.1175/1520-0442(1992)005<0541:AIOMFF>2.0.CO;2.

Brooks, I. H., and P. P. Niiler, 1977: Energetics of the Florida current. *J. Mar. Res.*, **35**, 163–191.

Candela, J., J. Sheinbaum, J. Ochoa, A. Badan, and R. Leben, 2002: The potential vorticity flux through the Yucatan Channel and the Loop Current in the Gulf of Mexico. *Geophys. Res. Lett.*, **29**, 2059, https://doi.org/10.1029/2002GL015587.

Chang, Y.-L., and L.-Y. Oey, 2011: Loop Current cycle: Coupled response of the Loop Current with deep flows. *J. Phys. Oceanogr.*, **41**, 458–471, https://doi.org/10.1175/2010JPO4479.1.

——, and ——, 2013: Loop Current growth and eddy shedding using models and observations: Numerical process experiments and satellite altimetry data. *J. Phys. Oceanogr.*, **43**, 669–689, https://doi.org/10.1175/JPO-D-12-0139.1.

Chérubin, L. M., Y. Morel, and E. P. Chassignet, 2006: Loop Current ring shedding: The formation of cyclones and the effect of topography. *J. Phys. Oceanogr.*, **36**, 569–591, https://doi.org/10.1175/JPO2871.1.

Chiri, H., A. J. Abascal, S. Castanedo, J. A. A. Antolínez, Y. Liu, R. H. Weisberg, and R. Medina, 2019: Statistical simulation of ocean current patterns using autoregressive logistic regression models: A case study in the Gulf of Mexico. *Ocean Modell.*, **136**, 1–12, https://doi.org/10.1016/j.ocemod.2019.02.010.

Cochrane, J. D., 1972: Separation of an anticyclone and subsequent developments in the Loop Current. *Contributions on the Physical Oceanography of the Gulf of Mexico*, L. R. A. Capuro and J. L. Reid, Eds., Gulf Publishing, 91–106.

Cox, M. D., 1980: Generation and propagation of 30-day waves in a numerical model of the Pacific. *J. Phys. Oceanogr.*, **10**, 1168–1186, https://doi.org/10.1175/1520-0485(1980)010<1168:GAPODW>2.0.CO;2.

Donohue, K. A., D. R. Watts, P. Hamilton, R. Leben, and M. Kennelly, 2016: Loop Current eddy formation and baroclinic instability. *Dyn. Atmos. Oceans*, **76**, 195–216, https://doi.org/10.1016/j.dynatmoce.2016.01.004.

Ertel, H., 1942: Ein neuer hydrodynamischer Erhaltungssatz. *Naturwissenschaften*, **30**, 543–544, https://doi.org/10.1007/BF01475602.

Fratantoni, P. S., T. N. Lee, G. P. Podesta, and F. Muller-Karger, 1998: The influence of Loop Current perturbations on the formation and evolution of Tortugas eddies in the southern Straits of Florida. *J. Geophys. Res.*, **103**, 24 759–24 779, https://doi.org/10.1029/98JC02147.

Garcia-Jove, M., J. Sheinbaum, and J. Jouanno, 2016: Sensitivity of Loop Current metrics and eddy detachments to different model configurations: The impact of topography and Caribbean perturbations. *Atmósfera*, **29**, 235–265, https://doi.org/10.20937/ATM.2016.29.03.05.

Gopalakrishnan, G., B. D. Cornuelle, and I. Hoteit, 2013a: Adjoint sensitivity studies of Loop Current and eddy shedding in the Gulf of Mexico. *J. Geophys. Res. Oceans*, **118**, 3315–3335, https://doi.org/10.1002/jgrc.20240.

——, ——, ——, D. L. Rudnick, and W. B. Owens, 2013b: State estimates and forecasts of the Loop Current in the Gulf of Mexico using the MITgcm and its adjoint. *J. Geophys. Res. Oceans*, **118**, 3292–3314, https://doi.org/10.1002/jgrc.20239.

Hamilton, P., A. Lugo-Fernández, and J. Sheinbaum, 2016: A Loop Current experiment: Field and remote measurements. *Dyn. Atmos. Oceans*, **76**, 156–173, https://doi.org/10.1016/j.dynatmoce.2016.01.005.

——, A. Bower, H. Furey, R. Leben, and P. Pérez-Brunius, 2019: The Loop Current: Observations of deep eddies and topographic waves. *J. Phys. Oceanogr.*, **49**, 1463–1483, https://doi.org/10.1175/JPO-D-18-0213.1.

He, R., and R. H. Weisberg, 2003: A loop current intrusion case study on the West Florida Shelf. *J. Phys. Oceanogr.*, **33**, 465–477, https://doi.org/10.1175/1520-0485(2003)033<0465:ALCICS>2.0.CO;2.

Hetland, R. D., Y. Hsueh, R. R. Leben, and P. P. Niiler, 1999: A Loop Current-induced jet along the edge of the West Florida Shelf. *Geophys. Res. Lett.*, **26**, 2239–2242, https://doi.org/10.1029/1999GL900463.

Hong, X., S. W. Chang, S. Raman, L. K. Shay, and R. Hodur, 2000: The interaction between Hurricane Opal (1995) and a warm core ring in the Gulf of Mexico. *Mon. Wea. Rev.*, **128**, 1347–1365, https://doi.org/10.1175/1520-0493(2000)128<1347:TIBHOA>2.0.CO;2.

Hoteit, I., T. Hoar, G. Gopalakrishnan, N. Collins, J. Anderson, B. Cornuelle, A. Köhl, and P. Heimbach, 2013: A MITgcm/DART ensemble analysis and prediction system with application to the Gulf of Mexico. *Dyn. Atmos. Oceans*, **63**, 1–23, https://doi.org/10.1016/j.dynatmoce.2013.03.002.

Huang, H., N. D. Walker, Y. Hsueh, Y. Chao, and R. R. Leben, 2013: An analysis of loop current frontal eddies in a 1/6° Atlantic Ocean model simulation. *J. Phys. Oceanogr.*, **43**, 1924–1939, https://doi.org/10.1175/JPO-D-12-0227.1.

Hurlburt, H. E., and J. D. Thompson, 1980: A numerical study of loop current intrusions and eddy shedding. *J. Phys. Oceanogr.*, **10**, 1611–1651, https://doi.org/10.1175/1520-0485(1980)010<1611:ANSOLC>2.0.CO;2.

——, and ——, 1982: The dynamics of the Loop Current and shed eddies in a numerical model of the Gulf of Mexico. *Hydrodynamics of Semi-Enclosed Seas*, J. C. J. Nihoul, Ed., Elsevier Oceanography Series, Vol. 34, Elsevier Scientific, 243–297.

Jaimes, B., L. K. Shay, and J. K. Brewster, 2016: Observed air-sea interactions in tropical cyclone Isaac over Loop Current mesoscale eddy features. *Dyn. Atmos. Oceans*, **76**, 306–324, https://doi.org/10.1016/j.dynatmoce.2016.03.001.

Jouanno, J., J. Ochoa, E. Pallàs-Sanz, J. Sheinbaum, F. Andrade-Canto, J. Candela, and J.-M. Molines, 2016: Loop Current frontal eddies: Formation along the Campeche Bank and impact of coastally trapped waves. *J. Phys. Oceanogr.*, **46**, 3339–3363, https://doi.org/10.1175/JPO-D-16-0052.1.

LaCasce, J. H., J. Escartin, E. P. Chassignet, and X. Xu, 2019: Jet instability over smooth, corrugated, and realistic bathymetry. *J. Phys. Oceanogr.*, **49**, 585–605, https://doi.org/10.1175/JPO-D-18-0129.1.

Leben, R. R., 2005: Satellite observations of Gulf of Mexico mesoscale circulation and variability. *Circulation in the Gulf of Mexico: Observations and Models, Geophys. Monogr.*, Vol. 161, Amer. Geophys. Union, 181–201.

Le Hénaff, M., V. H. Kourafalou, Y. Morel, and A. Srinivasan, 2012: Simulating the dynamics and intensification of cyclonic Loop Current frontal eddies in the Gulf of Mexico. *J. Geophys. Res.*, **117**, C02034, https://doi.org/10.1029/2011JC007279.

Liang, X. S., 2016: Canonical transfer and multiscale energetics for primitive and quasigeostrophic atmospheres. *J. Atmos. Sci.*, **73**, 4439–4468, https://doi.org/10.1175/JAS-D-16-0131.1.

——, and A. R. Robinson, 2005: Localized multiscale energy and vorticity analysis: I. Fundamentals. *Dyn. Atmos. Oceans*, **38**, 195–230, https://doi.org/10.1016/j.dynatmoce.2004.12.004.

——, and D. G. M. Anderson, 2007: Multiscale window transform. *Multiscale Model. Simul.*, **6**, 437–467, https://doi.org/10.1137/06066895X.

——, and A. R. Robinson, 2007: Localized multi-scale energy and vorticity analysis: II. Finite-amplitude instability theory and validation. *Dyn. Atmos. Oceans*, **44**, 51–76, https://doi.org/10.1016/j.dynatmoce.2007.04.001.

Lin, Y., R. J. Greatbatch, and J. Sheng, 2010: The influence of Gulf of Mexico Loop Current intrusion on the transport of the Florida current. *Ocean Dyn.*, **60**, 1075–1084, https://doi.org/10.1007/s10236-010-0308-0.

Liu, Y., X. S. Liang, and R. H. Weisberg, 2007: Rectification of the bias in the wavelet power spectrum. *J. Atmos. Oceanic Technol.*, **24**, 2093–2102, https://doi.org/10.1175/2007JTECHO511.1.

——, R. H. Weisberg, J. M. Lenes, L. Zheng, K. Hubbard, and J. J. Walsh, 2016a: Offshore forcing on the "pressure point" of the West Florida Shelf: Anomalous upwelling and its influence on harmful algal blooms. *J. Geophys. Res. Oceans*, **121**, 5501–5515, https://doi.org/10.1002/2016JC011938.

——, ——, S. Vignudelli, and G. T. Mitchum, 2016b: Patterns of the Loop Current system and regions of sea surface height variability in the eastern Gulf of Mexico revealed by the self-organizing maps. *J. Geophys. Res. Oceans*, **121**, 2347–2366, https://doi.org/10.1002/2015JC011493.

Lorenz, E. N., 1955: Available potential energy and the maintenance of the general circulation. *Tellus*, **7**, 157–167, https://doi.org/10.3402/tellusa.v7i2.8796.

Lugo-Fernández, A., and R. R. Leben, 2010: On the linear relationship between Loop Current retreat latitude and eddy separation period. *J. Phys. Oceanogr.*, **40**, 2778–2784, https://doi.org/10.1175/2010JPO4354.1.

——, ——, and C. A. Hall, 2016: Kinematic metrics of the Loop Current in the Gulf of Mexico from satellite altimetry. *Dyn. Atmos. Oceans*, **76**, 268–282, https://doi.org/10.1016/j.dynatmoce.2016.01.002.

Marshall, J., A. Adcroft, C. Hill, L. Perelman, and C. Heisey, 1997: A finite-volume, incompressible Navier Stokes model for studies of the ocean on parallel computers. *J. Geophys. Res.*, **102**, 5753–5766, https://doi.org/10.1029/96JC02775.

Masina, S., S. G. H. Philander, and A. B. G. Bush, 1999: An analysis of tropical instability waves in a numerical model of the Pacific Ocean: 2. Generation and energetics of the waves. *J. Geophys. Res.*, **104**, 29 637–29 661, https://doi.org/10.1029/1999JC900226.

Meza-Padilla, R., C. Enriquez, Y. Liu, and C. M. Appendini, 2019: Ocean circulation in the western Gulf of Mexico using self-organizing maps. *J. Geophys. Res. Oceans*, **124**, 4152–4167, https://doi.org/10.1029/2018JC014377.

Molina, M. J., R. P. Timmer, and J. T. Allen, 2016: Importance of the Gulf of Mexico as a climate driver for U.S. severe thunderstorm activity. *Geophys. Res. Lett.*, **43**, 12 295–12 304, https://doi.org/10.1002/2016GL071603.

Molinari, R. L., J. F. Festa, and D. W. Behringer, 1978: The circulation in the Gulf of Mexico derived from estimated dynamic height fields. *J. Phys. Oceanogr.*, **8**, 987–996, https://doi.org/10.1175/1520-0485(1978)008<0987:TCITGO>2.0.CO;2.

Morey, S. L., and Coauthors, 2020: Assessment of numerical simulations of deep circulation and variability in the Gulf of Mexico using recent observations. *J. Phys. Oceanogr.*, **50**, 1045–1064, https://doi.org/10.1175/JPO-D-19-0137.1.

Moum, J. N., D. R. Caldwell, J. D. Nash, and G. D. Gunderson, 2002: Observations of boundary mixing over the continental slope. *J. Phys. Oceanogr.*, **32**, 2113–2130, https://doi.org/10.1175/1520-0485(2002)032<2113:OOBMOT>2.0.CO;2.

Murphy, S. J., H. E. Hurlburt, and J. J. O'Brien, 1999: The connectivity of eddy variability in the Caribbean Sea, the Gulf of Mexico, and the Atlantic Ocean. *J. Geophys. Res.*, **104**, 1431–1453, https://doi.org/10.1029/1998JC900010.

Nash, J. D., E. Kunze, J. M. Toole, and R. W. Schmitt, 2004: Internal tide reflection and turbulent mixing on the continental slope. *J. Phys. Oceanogr.*, **34**, 1117–1134, https://doi.org/10.1175/1520-0485(2004)034<1117:ITRATM>2.0.CO;2.

National Academies of Sciences, Engineering and Medicine, 2018: *Understanding and Predicting the Gulf of Mexico Loop Current: Critical Gaps and Recommendations*. National Academies Press, 116 pp.

Nof, D., 2005: The momentum imbalance paradox revisited. *J. Phys. Oceanogr.*, **35**, 1928–1939, https://doi.org/10.1175/JPO2772.1.

Oey, L.-Y., 2004: Vorticity flux through the Yucatan Channel and Loop Current variability in the Gulf of Mexico. *J. Geophys. Res.*, **109**, C10004, https://doi.org/10.1029/2004JC002400.

——, 2008: Loop Current and deep eddies. *J. Phys. Oceanogr.*, **38**, 1426–1449, https://doi.org/10.1175/2007JPO3818.1.

Pedlosky, J., 1987: *Geophysical Fluid Dynamics*. 2nd ed. Springer-Verlag, 710 pp.

Pérez-Brunius, P., H. Furey, A. Bower, P. Hamilton, J. Candela, P. García-Carrillo, and R. Leben, 2018: Dominant circulation patterns of the deep Gulf of Mexico. *J. Phys. Oceanogr.*, **48**, 511–529, https://doi.org/10.1175/JPO-D-17-0140.1.

Pichevin, T., and D. Nof, 1997: The momentum imbalance paradox. *Tellus*, **49A**, 298–319, https://doi.org/10.3402/tellusa.v49i2.14484.

Qiao, L., and R. H. Weisberg, 1998: Tropical instability wave energetics: Observations from the tropical instability wave experiment. *J. Phys. Oceanogr.*, **28**, 345–360, https://doi.org/10.1175/1520-0485(1998)028<0345:TIWEOF>2.0.CO;2.

Reid, R. O., 1972: A simple dynamic model of the Loop Current. *Contributions to the Physical Oceanography of the Gulf of Mexico*, L. R. A. Capurro and J. L. Reid, Eds., Texas A&M University Oceanographic Studies, Vol. 2, Gulf Publishing, 157–159.

Rosburg, K. C., K. A. Donohue, and E. P. Chassignet, 2016: Three-dimensional model-observation comparison in the Loop Current region. *Dyn. Atmos. Oceans*, **76**, 283–305, https://doi.org/10.1016/j.dynatmoce.2016.05.001.

Rudnick, D. L., G. Gopalakrishnan, and B. D. Cornuelle, 2015: Cyclonic eddies in the Gulf of Mexico: Observations by underwater gliders and simulations by numerical model. *J. Phys. Oceanogr.*, **45**, 313–326, https://doi.org/10.1175/JPO-D-14-0138.1.

Schmitz, W. J., Jr., 2005: Cyclones and westward propagation in the shedding of anticyclonic rings from the Loop Current. *Circulation in the Gulf of Mexico: Observations and Models, Geophys. Monogr.*, Vol. 161, Amer. Geophys. Union, 241–261.

Sérazin, G., T. Penduff, B. Barnier, J.-M. Molines, B. K. Arbic, M. Müller, and L. Terray, 2018: Inverse cascades of kinetic energy as a source of intrinsic variability: A global OGCM study. *J. Phys. Oceanogr.*, **48**, 1385–1408, https://doi.org/10.1175/JPO-D-17-0136.1.

Shay, L. K., 2019: Upper ocean structure: Responses to strong atmospheric forcing events. *Encyclopedia of Ocean Sciences*, 3rd ed. J. K. Cochran, H. J. Bokuniewicz, and P. L. Yager, Eds., Academic Press, 86–96.

Sheinbaum, J., G. Athié, J. Candela, J. Ochoa, and A. Romero-Arteaga, 2016: Structure and variability of the Yucatan and Loop Currents along the slope and shelf break of the Yucatan Channel and Campeche bank. *Dyn. Atmos. Oceans*, **76**, 217–239, https://doi.org/10.1016/j.dynatmoce.2016.08.001.

Sturges, W., and R. R. Leben, 2000: Frequency of ring separations from the Loop Current in the Gulf of Mexico: A revised estimate. *J. Phys. Oceanogr.*, **30**, 1814–1819, https://doi.org/10.1175/1520-0485(2000)030<1814:FORSFT>2.0.CO;2.

von Storch, J.-S., C. Eden, I. Fast, H. Haak, D. Hernández-Deckers, E. Maier-Reimer, J. Marotzke, and D. Stammer, 2012: An estimate of the Lorenz energy cycle for the world ocean based on the STORM/NCEP simulation. *J. Phys. Oceanogr.*, **42**, 2185–2205, https://doi.org/10.1175/JPO-D-12-079.1.

Vukovich, F. M., 2007: Climatology of ocean features in the Gulf of Mexico using satellite remote sensing data. *J. Phys. Oceanogr.*, **37**, 689–707, https://doi.org/10.1175/JPO2989.1.

——, and G. A. Maul, 1985: Cyclonic eddies in the eastern Gulf of Mexico. *J. Phys. Oceanogr.*, **15**, 105–117, https://doi.org/10.1175/1520-0485(1985)015<0105:CEITEG>2.0.CO;2.

Walker, N. D., R. R. Leben, S. Anderson, J. Feeney, P. Coholan, and N. Sharma, 2009: Loop Current frontal eddies based on satellite remote sensing and drifter data. U.S. Department of the Interior Minerals Management Service Rep. OCS Study MMS 2009-023, 78 pp., https://digital.library.unt.edu/ark:/67531/metadc955819/m2/1/high_res_d/4839.pdf.

——, and Coauthors, 2011: Impacts of a Loop Current frontal eddy cyclone and wind forcing on the 2010 Gulf of Mexico oil spill. *Monitoring and Modeling the Deepwater Horizon Oil Spill: A Record-Breaking Enterprise, Geophys. Monogr.*, Vol. 195, Amer. Geophys. Union, 103–116.

Weisberg, R. H., and T. J. Weingartner, 1988: Instability waves in the equatorial Atlantic Ocean. *J. Phys. Oceanogr.*, **18**, 1641–1657, https://doi.org/10.1175/1520-0485(1988)018<1641:IWITEA>2.0.CO;2.

——, and R. He, 2003: Local and deep-ocean forcing contributions to anomalous water properties on the West Florida Shelf. *J. Geophys. Res.*, **108**, 3184, https://doi.org/10.1029/2002JC001407.

——, and Y. Liu, 2017: On the Loop Current penetration into the Gulf of Mexico. *J. Geophys. Res. Oceans*, **122**, 9679–9694, https://doi.org/10.1002/2017JC013330.

Xu, F.-H., Y.-L. Chang, L.-Y. Oey, and P. Hamilton, 2013: Loop Current growth and eddy shedding using models and observations: Analyses of the July 2011 eddy-shedding event. *J. Phys. Oceanogr.*, **43**, 1015–1027, https://doi.org/10.1175/JPO-D-12-0138.1.

Yang, Y., and X. S. Liang, 2019a: New perspectives on the generation and maintenance of the Kuroshio large meander. *J. Phys. Oceanogr.*, **49**, 2095–2113, https://doi.org/10.1175/JPO-D-18-0276.1.

——, and ——, 2019b: Spatiotemporal variability of the global ocean internal processes inferred from satellite observations. *J. Phys. Oceanogr.*, **49**, 2147–2164, https://doi.org/10.1175/JPO-D-18-0273.1.

Yu, Z., J. P. McCreary, and J. A. Proehl, 1995: Meridional Asymmetry and energetics of tropical instability waves. *J. Phys. Oceanogr.*, **25**, 2997–3007, https://doi.org/10.1175/1520-0485(1995)025<2997:MAAEOT>2.0.CO;2.

Zhai, X., and D. P. Marshall, 2013: Vertical eddy energy fluxes in the North Atlantic subtropical and subpolar gyres. *J. Phys. Oceanogr.*, **43**, 95–103, https://doi.org/10.1175/JPO-D-12-021.1.

Zhang, Y., C. Hu, Y. Liu, R. H. Weisberg, and V. H. Kourafalou, 2019: Submesoscale and mesoscale eddies in the Florida Straits: Observations from satellite ocean color measurements. *Geophys. Res. Lett.*, **46**, 13 262–13 270, https://doi.org/10.1029/2019GL083999.